INTERACTION BETWEEN HEPARIN AND THE ROUNDABOUT RECEPTOR AT THE SINGLE-MOLECULE LEVEL

by

R. ALEXANDER REESE

(Under the Direction of Bingqian Xu)

ABSTRACT

Atomic force microscopy has advanced to the point that in situ measurements of biological systems can be made at the single-molecule level, providing information on rare states that are lost in standard ensemble measurements and allowing specific detection of proteins and polysaccharides. One such system is that of the signaling pathway Slit-Roundabout (Robo), which has been implicated in the development of the nervous system, heart, and cancer. The Slit-Robo complex is stabilized and regulated by heparan sulfate (HS), a linear, structurally-heterogeneous polysaccharide expressed widely on mammalian cell membranes. Thus, better understanding of HS's regulatory role could allow us to target therapies related to this pathway. Using dynamic force spectroscopic methods, this research shows that is possible to create a model system allowing for the measurement of single-molecule interactions between the HS variant heparin and the Robo1 protein, elucidating the kinetics of the interaction using the entire polysaccharide in ambient conditions.

INDEX WORDS: heparan sulfate, Roundabout receptor, AFM, single-molecule, force spectroscopy, recognition imaging

INTERACTION BETWEEN HEPARIN AND THE ROUNDABOUT RECEPTOR AT THE SINGLE-MOLECULE LEVEL

by

R. ALEXANDER REESE

B.S., University of Georgia, 2013

A Thesis Submitted to the Graduate Faculty of The University of Georgia in Partial Fulfillment of the Requirements for the Degree

MASTER OF SCIENCE

ATHENS, GEORGIA

2019

INTERACTION BETWEEN HEPARIN AND THE ROUNDABOUT RECEPTOR AT THE SINGLE-MOLECULE LEVEL

by

R. ALEXANDER REESE

Major Professor:	Bingqian Xu
Committee:	Jason Locklin
	Sergiy Minko

Electronic Version Approved:

Suzanne Barbour
Dean of the Graduate School
The University of Georgia
August 2019

ACKNOWLEDGEMENTS

Many people have helped me reach where I am. First, thank you to my parents, who were my first supporters and remain behind me still, a far longer time than I would have granted myself. Thanks too to my wife, Heidi, who has provided me throughout graduate school with thoughtful advice and relaxing company.

Special thanks to my lab mates Tong Zhang, Kun Wang, and Yangang Pan for their considerable help training me. And thank you too to Ran Zhang, Ran Liu, and Sneha Kandapal for your friendship, without which graduate school would have been a much gloomier place.

Finally, thank you to my advisor, Dr. Bingqian Xu, for giving me the opportunity to do this research, supporting me academically and financially. I will always remain grateful for that.

TABLE OF CONTENTS

Page

LIST OF FIGURES

Page

CHAPTER 1

INTRODUCTION

1.1 Cell signaling and glycobiology

The ability to respond to stimuli is a fundamental and defining aspect of life. The most basic unit capable of achieving this feat is the cell, and the multidisciplinary field studying its ability to interact and communicate with its environment is referred to as cell signaling. Cell signaling is vital to maintaining all the processes incumbent on cells to maintain life: finding nutrients, avoiding environmental stresses or predators, and monitoring internal states such as homeostasis and the cell cycle[1]. These signals can be physical in nature, such as changes in light, pH, or temperature; or they can be more complex molecular events, such as the recognition of antigens of an invading cell. In either event, cells must appropriately recognize the signal, detecting it even among myriad and contradictory inputs; transduce the signal into an action within the cell[2], such as a change in the transcription and translation processes leading to differential protein output or a modification of the cytoskeleton to effect a change in cellular transportation or cell motility[3]; and finally, it must tightly regulate the entire pathway, given the biological imperative to react robustly yet efficiently.

Furthermore, in multicellular organisms, these processes grow even more complex, as cells must coordinate with other cells of differentiated function, sometimes across distances reaching the order of meters[2]. These cells are organized into increasingly differentiated functions as one climbs up the evolutionary tree, with higher organisms exhibiting organs solely dedicated to detecting external stimuli (the eye, the ear, the nose) and then passing that information along

through the nervous system, so the organism can appropriately respond. This extracellular signaling is frequently achieved through protein interactions, wherein an extracellular recognition event is transduced into signal within the cell[4]. And to add further complication, the conjugation of these proteins and their ligands with carbohydrate moieties to form glycoconjugates (Fig. 1) further encodes signaling information and regulates the interactions. Such molecular interactions arise from noncovalent bonds and are essential to understanding biological recognition and signaling[5]. More recently, the apparent contradiction between the importance of these interactions and the relative weaknesses of the protein-carbohydrate intermolecular forces causing them has given rise to the multivalency explanation[6-7], wherein multiple iterations of the same ligands and receptors create sufficient avidity so as to impart physiologically relevant forces on the involved constituents.

Fundamentally, these cellular signaling systems are systems of information processing, albeit ones of evolved design and extreme complexity, and thus, current tools remain insufficient to quickly and comprehensively dissect the full functions of cell signaling[8-9]. Large genomic screening has had some success in increasing the field's productivity, but much work still proceeds via knock-out experiments.

Glycoconjugates stabilize the matrix for other biomolecules in addition to encoding information that regulates cell signaling[10]. Much of this is owed to the vast heterogeneity of glycosylated products. Unlike other biological macromolecules such as proteins and nucleic acids, the carbohydrate space is not synthesized in a fully template-driven manner. Each monosaccharaide component in a polysaccharide is subject to be a branch point, have different chemistry about its anomeric center, have different glyosidic linkages, or feature different types of sulfation or acetylation[11]. This results in tremendous structural variability which frustrates

determination of structure-activity relationships. Even small differences can cause significant changes in their biochemical functionality, although whether these are fully deterministic processes remains unresolved, as changes sometimes result in negligible biochemical outcomes. The field remains mostly unexplored, and this lack of understanding of the structure-function relationship stems directly from a dearth of well-developed and widely-implementable tools[12-14]. With time, increased ability to sequence sugars and determine binding sites between carbohydrates and their conjugates will surely elucidate the processes involved in glycobiology.

This is important because identifying these pathways and being able to determine the glycopharmacophore ought to pave the way to make these pathways and processes druggable, as is the case in recent work being done to develop vaccines on the basis of carbohydrate chemistry instead of conventional protein chemistry[15-17].

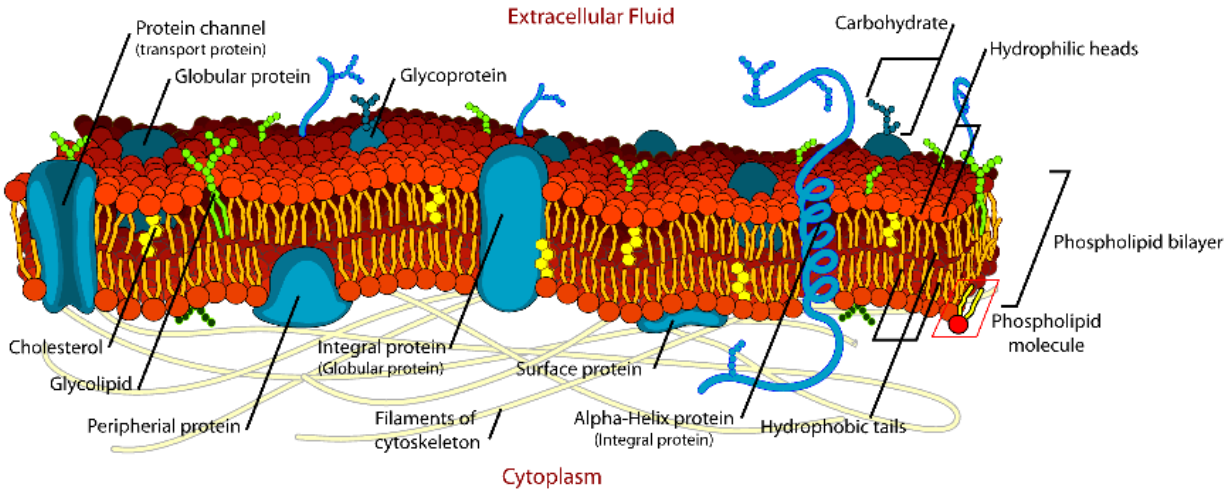

Figure 1. A cartoon depiction of a cell membrane. Carbohydrate moieties decorate and modulate various proteins and lipids on the surface. Image reproduced under the GNU Free Documentation License, v.1.2.

1.2 The Slit Robo complex and heparan sulfate

One such protein interaction that has attracted significant attention over the past three decades is that of the Slit and Roundabout (Robo) system. Robo is a transmembrane receptor whose gene was initially discovered in Drosophila by Seeger and coworkers in 1993[18]. During a large-scale screening for genes that affect CNS development, they hit upon the robo gene, showing that it was responsible for preventing developing axons from re-crossing the midline during development (it would turn around upon approaching the midline, hence the name Roundabout). Its ligand, Slit, was discovered six years later by Brose and coworkers[19] in the extracellular space around glial cells in the midline. It is a glycoprotein, glycosylated within and secreted from the Golgi apparatus. It consists of a highly conserved N-terminus signaling peptide followed by four leucine-rich repeat (LRR) domains, a series of epidermal growth factor (EGF)-like domains, and a G-like domain. There are then a variable number of EGF-like domains depending on species, before the peptide ends at the C-terminal with a cysteine knot[19] (Fig. 2A). Slit binds to Robo through its LRR domain, wherein Robo transduces the signal into a modification of the actin cytoskeleton, which causes a change in cell motility[20-21].

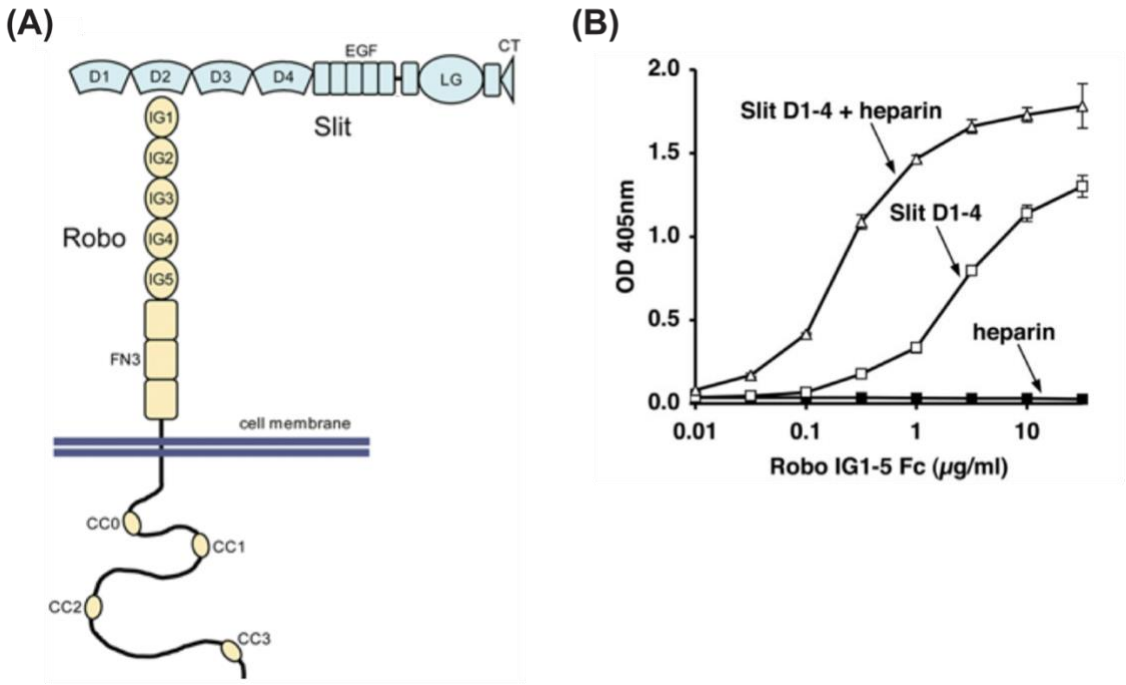

Figure 2. Robo and Slit's domain structure and their increased affinity in the presence of heparin. (A) A cartoon depiction of Robo and Slit, showing their basic domain structures and their interaction between the LRR domains of Slit and the Ig domains of Robo. Adapted from Hohenester[22] with permission. (B) Binding assay showing the increased binding of Robo by immobilizaed Slit in the presence of heparin. Reproduced with permission from Hussain and coworkers[23].

Since its discovery as a contributor to axon guidance, the system has been found to modulate various other developing tissues in the same chemorepellent manner. These include angiogenesis[24-25], tumorigenesis[26], and cardiac development[27]. In all these systems, Slit is expressed in the extracellular matrix in gradients, leading to Robo-expressing tissues to be guided away from the higher concentrations of Slit (Fig. 3). Robust understanding of this signaling pathway will thus provide the ability to exert a significant degree of control over developing tissues and the diseases that affect them.

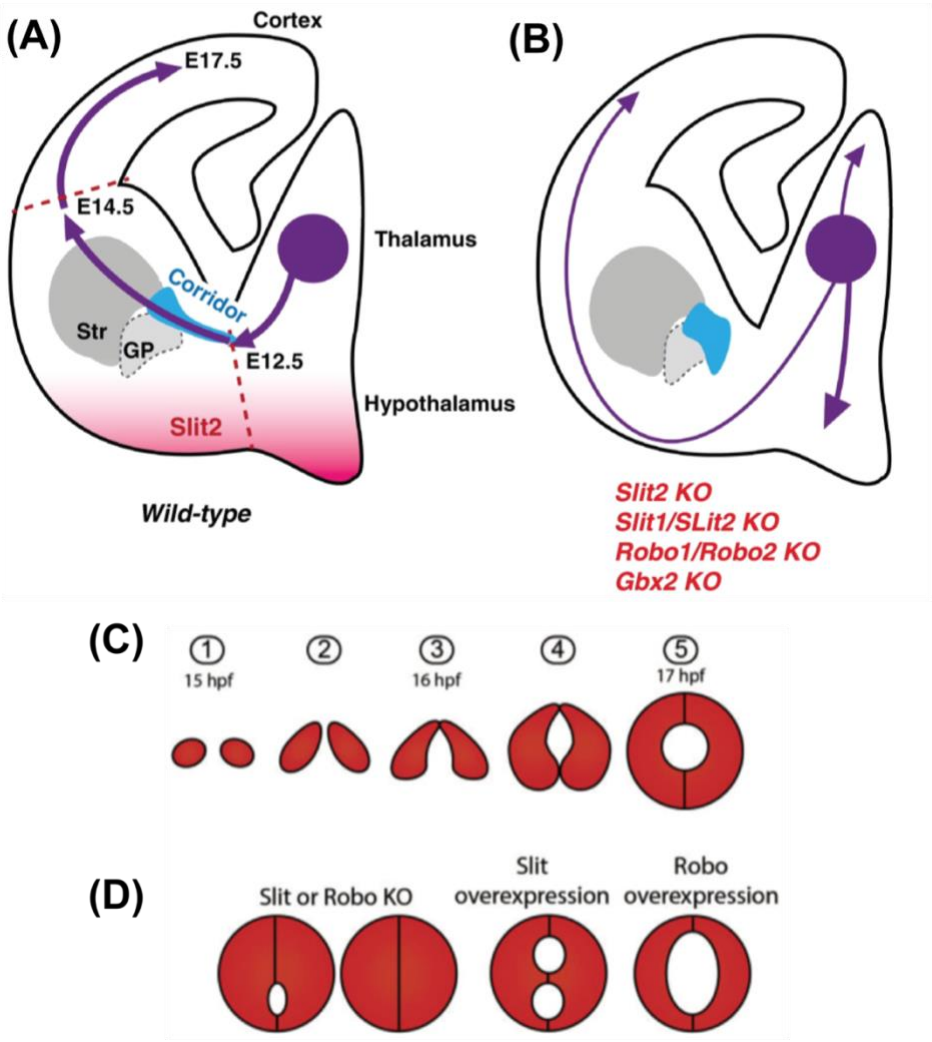

Figure 3. Examples of the importance of the Slit-Robo pathway in tissue and organ development. (A) Neurons in the developing brain are steered by the presence of a Slit gradient, but (B) a knockout of either Slit or Robo results in aberrant development. Reproduced with permission from Blokus and Chédotal[28]. (C) The development of the lumen in the development of the *Drosophila* heart from 15-17 hours past fertilization (hpf) is ensured by the Slit-Robo chemorepulsion. (D) Aberrant expression of either Slit or Robo results in defective lumen formation. Reproduced under the Creative Commons CC BY license from Zhao and Mommersteeg[27].

One well-studies class of sugars found to modulate these Robo-Slit interactions is that of heparan sulfate. These are highly acidic, linear polysaccharides within the glycosaminoglycan

(GAG) family. The most common disaccharide unit of HS is that of glucuronic or idouronic acid and glycosaminoglycan (Fig. 4A). As polysaccharide chain elongation occurs, various post-synthetic modifications are made in the Golgi apparatus such as O-sulfation, N-deacetylation and sulfation, and epimerization of glucruonic acid into iduronic acid at the C-5 position[29]. These modifications often form regions or domains along the length of the polysaccharide chain (Fig. 4B) with variably higher or lower degrees of sulfation and thus varying charge density. This domain structure is believed to impart the sugar's ability to bind and regulate proteins, where HS serves as a cofactor for protein signaling pathways including fibroblast growth factor signaling[30]; Wnt signaling[31]; and Slit-Robo signaling, where studies[21, 23, 32-33] have shown that heparin helps stabilize the Slit-Robo complex (Fig. 2B), promoting the chemorepellent interaction by effecting a reorganization of the cytoskeleton. Heparin is a heparan sulfate derivative consisting of less structurally-heterogeneous, highly sulfated polysaccharide chains, with an average charge of -1.7/monosaccharide[34]. In the body, it is sequestered in mast cells, so its ability to mimic HS is considered incidental, but it is readily harvested and thus amenable for experimental uses, and several heparin variants are currently involved in drug trials[34]. Challenges persist in the use of fully heterogeneous HS for experiments due to the difficulty of its synthesis[35] and the fact that heparin binding strength is determined by attachment modality[36].

Understanding the role that HS plays in modulating the effects of Slit-Robo is part of the burgeoning field of glycobiology, where the effects of sugars, their conjugated macromolecules, and the regulatory effects they exert on biological pathways, the so-called biological fine control, are being studied. Citations for the topic "glycobiology" grew five-fold since 2000 and exceeded 5,000/year in 2018 in Web of Science. That growth is being driven by the immense complexity

and importance[37-38] of glycosylation as a post-translational modification for proteins and as a ligand for proteins.

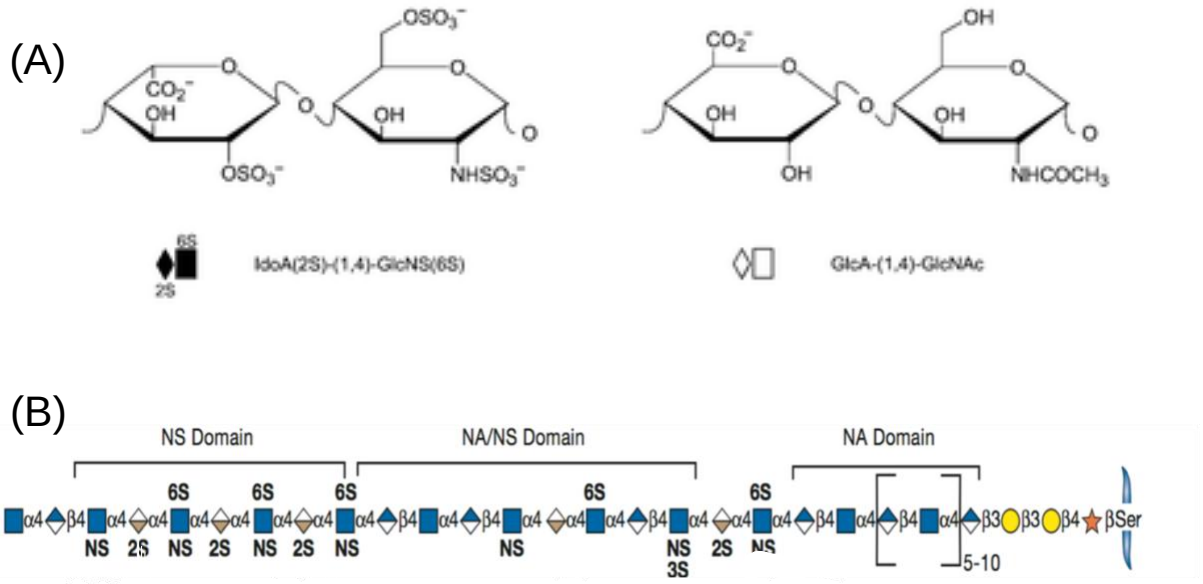

Figure 4. Structure of heparan sulfate proteoglycans. (A) The two most common disaccharide units comprising heparan sulfate. (B) A cartoon depiction of heparan sulfate-modified peptide, with the sulfation patterns denoted. Reproduced from Essentials of Glycobiology[39] with permission.

1.3 Current state of the field

The analysis of polysaccharides such as HS present significant challenges that exceed those of nucleic acids and proteins, both of which consist of a primary structure that can be precisely known and strongly predicts the molecule's structure under given conditions. Polysaccharides, by contrast, vary greatly in their linkage and stereochemistry[40]. Considerable analytical tools have been brought to bear on the problem of HS-Robo interactions, but routine analysis has remained elusive.

Chromatography-coupled mass spectrometry can elucidate sequence and composition in certain conditions[41], but high sulfation as in the case of HS leads to a high probability of in-source fragmentation, generally complicating spectral interpretation[42]. A detailed chemical shift

perturbation analysis with 2D $^{15}N-^{1}H$ HSQC NMR was used to develop a model of the binding between Robo1 and heparan sulfate[43]. And surface plasmon resonance has been used to probe bulk kinetics[44].

These methods have yielded considerable information on this system, but they have failed to provide a detailed mechanism for the interaction for full-length heparin. Here, it has been argued[45], lies a place for single-molecule methods to provide a path forward.

1.4 Single-molecule methods

Most analytical methods measure a property from a large ensemble of molecules, resulting in the measurement of an average property and giving rise to the peak shapes characteristic to analytical instrumentation. While this is often sufficient, there exist certain times when there is a marked advantage of measuring the discrete states of a system, including relatively rare states that may get wiped out in ensemble measurements; to be sure, sometimes these higher spatial and temporal resolutions are preferable. This is particularly useful when seeking measurements that necessitate challenging experimental conditions under ensemble averaged techniques, such as synchronizing all molecules under study, as is the case in the determination of time-dependent processes[3, 46-47]. Single-molecule measurements allow for the resolution of co-localized proteins[48-49], revealing the step motion and size of RNA polymerase's elongation action as being 3.4 Å[50-51], and confirming the codon as the unit for protein synthesis[52]. In all of these examples, the property measured from an ensemble would mask the interesting information in the spatially- or time-averaged property. Only single-molecule methods can faithfully capture this information because each measurement is on a single molecule in a discrete state. The hallmark of successful single molecule experiments is that an sufficiently high number of these measurements can, naturally, re-create the ensemble measurement provided that there exists an understanding of the underlying

principle of the group effects (such as understanding the diffraction-limited blurring of blue and yellow create green in reference 3), but information on the single molecule states is lost in an ensemble measurement[3].

More recently, the application of single-molecule methods to glycobiology is being recognized as a path forward for the field. Single-molecule methods' ability to interrogate rare events is useful in this context, providing mechanistic insight while ensemble methods merely show naïve interaction[53]. These methods can offer insight into structural as well as kinetic parameters of an interaction. This is seen in work by Martines and coworkers[54], where the degree of branching among oligosaccharides fragments interacting with anti-HIV 2G12 results in marked differences in lifetime, with the presence of a physiologically-relevant lifetime for variants containing at least three linear branches.

This can be seen in work to determine the interactions of ricin-antibody, where rare conformational states of the structure were observed, yet the overall parameters are in good agreement with that of bulk method SPR[55].

1.5 Atomic force microscopy

Scanning probe microscopy was introduced in 1982 with the scanning tunneling microscope[56], an instrument capable of imaging conductive surfaces with atomic resolution. The STM won the Nobel Prize in Physics in 1986, the same year its creators introduced the atomic force microscope (AFM), another SPM capable of imaging any surface[57]. AFM probes a surface with a flexible, sharp (~10 nm radius) probe mounted on the end of a cantilever that is raster-scanned across a surface to generate a three-dimensional image of the surface morphology[57]. A laser is shone onto the back of the cantilever and reflected onto a position sensitive photodetector (PSD). The tip is lowered into contact with the surface and raster-scanned across the surface, causing the cantilever

to flex in response to the changing topography, changing the deflection of the laser spot, which is recorded by the PSD. This deflection is the input of a feedback system that will re-establish an original value of laser deflection, known as the set point, by applying a voltage to a piezoelectric ceramic stack that controls the distance between the tip and the substrate. In recording the height at each point of the scan, an image can be reconstructed[58] (Fig. 5A). The high lateral forces exerted on the substrate as the tip is scanned across can damage of softer biological samples (Fig. 5B). Amplitude-modulated AFM (AM-AFM), commonly known as tapping mode (Fig. 5C), was developed to circumvent this problem. In AM-AFM, the tip is oscillated with a set free amplitude and is then lowered into contact with the surface, reducing the oscillation amplitude until it oscillates with a predetermined fraction of the free amplitude, at which the set point of the feedback system is established and maintained for the duration of the scan. Because the tip only intermittently contacts the surface and only applies a predominantly normal force, lateral forces are effectively eliminated[59]. This technique was later extended to liquid environments[60], establishing AFM as a capable tool for probing a broad range of biological samples in physiologically-relevant conditions[61].

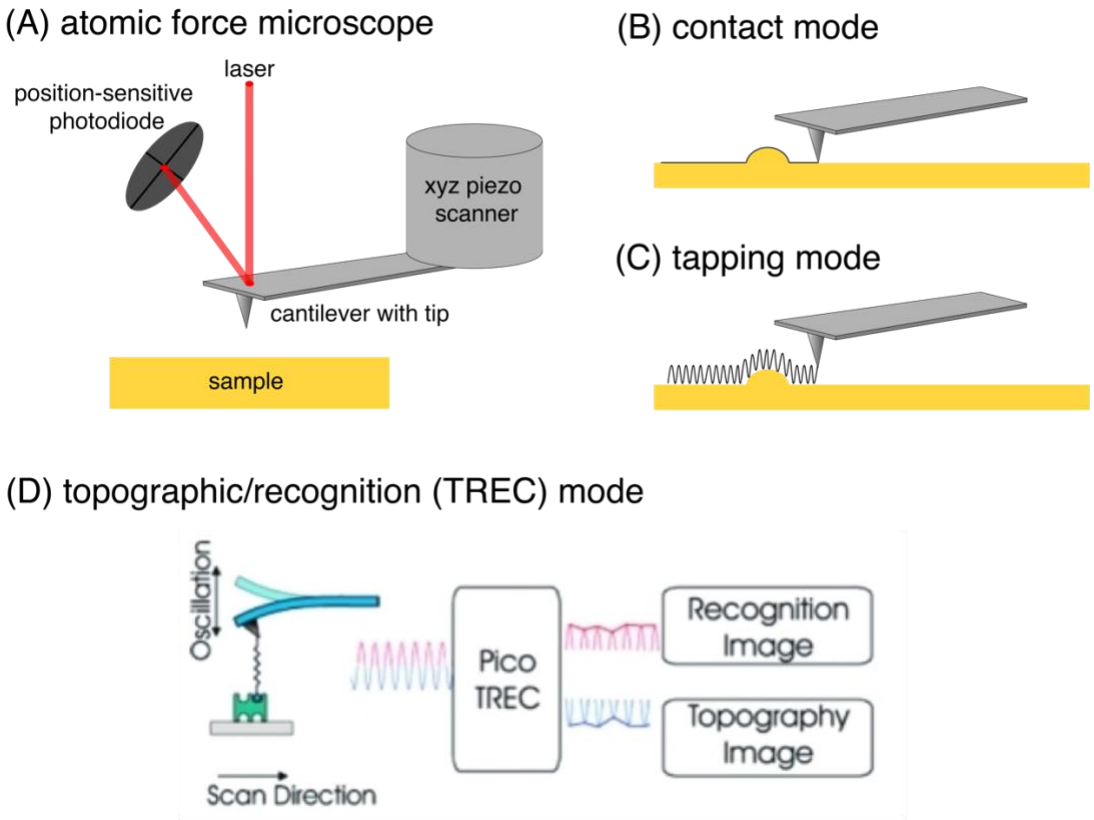

Figure 5. A schematic overview of AFM imaging modes. (A) A schematic of an AFM instrument. (B) Contact mode operation. (C) Tapping mode operation. (D) The TREC imaging process. The probe is driven in tapping mode as in C, but the upper and lower portions of the recorded signal are split by a PicoTREC controller and converted into the recognition and topographic images, respectively. Reproduced with permission from Ebner and coworkers[62].

The precise force applied by the AFM can be determined by finding the product of the sensitivity, the spring constant, and the displacement of the tip. The sensitivity of the cantilever is simply determined by recording a force-distance curve on a hard sample, yielding the change in voltage measured at the PSD against the change in piezo displacement, which on a hard surface indicates the distance the cantilever has flexed upward. A known sensitivity permits voltage differences, the sole read-out of an AFM, to be converted into cantilever displacements in the general context of experiments on all surfaces (Fig. 6A). From this point, straightforward

application of Hooke's Law permits the determination of the force, but first, the spring constant must be determined.

The standard methods of AFM probe manufacture are not capable of producing precisely identical probes. Rather, there is a tolerance within which the probes fall, which can exceed 100% error from the nominal value.

Several methods exist for determining the spring constant more accurately. The cantilever dimensions and material define the spring constant, so it is possible to determine k_c from them, but because k_c varies with the cube of the thickness, this method is prone to significant error if the cantilever cannot be precisely measured along its thinnest dimension. Reports exist of testing k_c against another cantilever of known k_c.

But by far, the most facile and accessible method is thermal tuning. Because the cantilever functions as an oscillator, its spring constant can be related to its power spectral density. By collecting a PSD at a known temperature, apodizing, and fitting a Lorentzian function to the peak, it is possible to elucidate the spring constant to a high degree of accuracy (Fig. 6B).

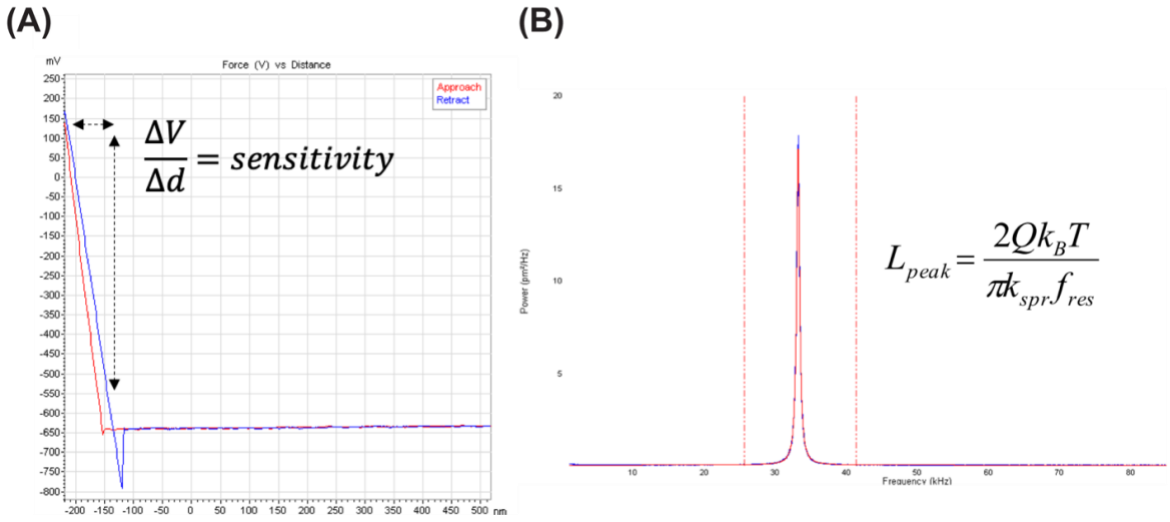

Figure 6. Calibrating the AFM cantilever to ensure accurate force measurements. (A) The sensitivity of the cantilever is determined by measuring a force-distance curve on a hard surface

and determining the slope of the curve in the contact regime. (B) The power spectral density is collected of a cantilever in ambient conditions. A Lorentzian fit of the peak permits determination of the spring constant.

AFM modes

The initial modality of AFM operation, contact mode, while revolutionary, imparts high lateral forces onto samples, precluding its use with soft or fragile samples, notably biological samples. In 1993, this issue was obviated by the introduction by Zhong and coworkers of the amplitude-modulation mode of AFM, commonly referred to as tapping mode[59]. Here, the probe cantilever's Hookean characteristics are exploited and the cantilever functions as an oscillator, driven my either an acoustic or magnetic signal. The oscillation achieves a set free amplitude, A_o, when driven at a resonant frequency which is dependent on the geometry of the cantilever and the mass of the tip. As the probe nears the sample surface, the tip begins to tap along the surface of the sample, reducing the free amplitude until some pre-established reduction of that free amplitude is achieved (this is usually set between 70-90% of A_o), which establishes the set point for the feedback control loop of the piezoelectric tube.

This was coupled with previous work permitting AFM operation in liquid conditions[60], and the modern incarnation of the AFM as a tool for biology was born. This ushered in a spate of achievements in biological microscopy and manipulation: native proteins, DNA, and cells were imaged[63]; sensing platforms for proteins and drugs were developed[64]; and nanomanipulation of proteins was achieved[65].

The resolution of AFM is theoretically higher than that of STM[66]. STM interacts with electrons at the Fermi level, whereas AFM is able to interact with all electrons in the molecule, including core electrons, which due to the uncertainty principle are more confined[67]. Achieving this is in

practice is challenging, however, because long-range forces rob resolving power and must be effectively managed, and the short-range forces, unlike in STM, are not monotonic[67] and can thus be challenging to build effective feedback mechanisms for. Nevertheless, the ability to resolve chemical bonds in aromatic systems under precisely controlled conditions (high vacuum, cryogenic temperatures) has been achieved in the last decade[68] and has been used to follow cyclization reactions on surfaces of ultraflat copper[66].

High-resolution imaging requires precise control over the tip-sample forces. The electrical double layer of the surface and tip can begin to interact around tens of nanometers[69]. Reducing this interaction by modifying pH or ionic concentration and achieving balanced electrostatic conditions has allowed for lateral resolution down to 0.6 nm on purple membrane[70].

Further progress toward AFM as a biological tool was made with the realization of adding the ability to record chemical data with AFM. Modification of the AFM probe tip with various functional groups ushered in chemical force microscopy, and further work allowed for the specific detection of interactions between tip- and surface-bound molecules with topographic/recognition imaging (TREC)[62] (Fig. 5D). TREC is a modified tapping imaging mode carried out in a liquid medium with a functionalized probe. Because of the liquid medium, the cantilever's oscillatory motion is overdamped. In its overdamped state, the peak and trough of the recorded sinusoidal signal of the cantilever's motion are effectively decoupled. The troughs respond, as expected in tapping mode, to rises and falls of the surface topography. But the peak of the signal remains unperturbed unless the upward motion of the cantilever is impeded by a molecular binding event between the functionalized molecule on the tip and its cognate ligand on the surface. Visually, these oscillatory impediment show up as dark regions in the recognition imaging channel. This

technique has been used to image the interactions between biotin-streptavidin[71], ricin-antibody[72], heparin-aptamer[73], DNA-binding proteins, and more[74].

Recently, significant developments have been achieved toward fixing a dogged problem of AFM since its inception: its relatively slow imaging speed of 2-10 min/frame. Slow imaging speeds categorically rule out the real-time observation of many biological processes that occur at the time scale of seconds or shorter. The high-speed AFM developed and improved upon by Ando and coworkers[75-76] has achieved imaging speeds on the order of 100 ms/frame, permitting real-time imaging of the translocation of myosin molecules along actin filaments[77], the "traffic jams" of cellulase on cellulose[78], the rotary motion of F1-ATPase catalysis[79], and the dynamics of CRISPR-Cas9 on DNA[80].

1.6 Single-molecule force spectroscopy

While initially developed as an instrument primarily focused on the imaging of surfaces, AFM's high lateral, temporal, and force resolution has provided a platform for an array of sophisticated bioanalytical and biophysical techniques that allow for specific chemical detection and the determination of kinetic and thermodynamic parameters of receptor ligand reactions and protein unfolding experiments: single-molecule force spectroscopy (SMFS or force spectroscopy).

The only read-out of an AFM is the recorded laser deflection, so to operationalize chemical detection, the AFM probe tip must be modified with a specific chemical moiety that will interact with a cognate receptor bound to the surface under study. In SMFS, the basic procedure involves sweeping a ligand chemically tethered to the probe into and out of contact with its cognate receptor on the surface. The pair stochastically binds as the tip presses into the surface and causes a repulsion to be observed in the spectrum. As the sweep reverses direction and the probe leaves contact with the surface, the bound ligand-receptor pair remains bound until the chemical linker is

pulled taught and the cantilever loads sufficient force to overcome the intermolecular forces comprising the ligand-receptor bond. The pair then ruptures, and this is observed as a sudden jump to the zero-force baseline of the spectrum (Fig. 7). This was first successfully demonstrated in an elegant study on the biotin-avidin complex[71], where the rupture force between the pair (known for its strong interactions) was measured at 160 ± 20 pN.

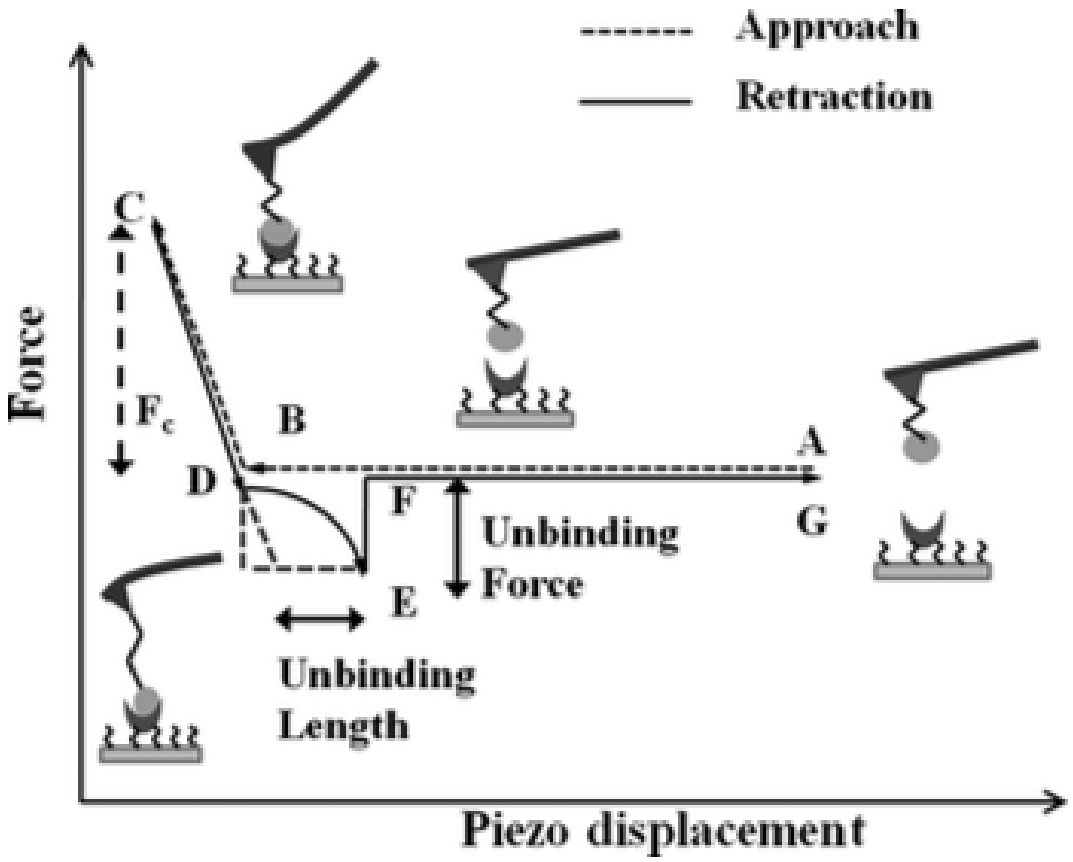

Figure 7. Schematic of a force-distance spectrum. (A) A molecule is chemically tethered to the end of the probe. The probe is then brought into contact with the surface and the molecule will bind its ligand. The sweep ends when the probe enters into the contact regime with the surface, and the probe begins retraction. The probe exits the contact regime and continues freely until the tether starts to become taught. As the polymer linker unwinds, it begins to exert a force on the cantilever which bends applying a Hookean force to the binding pair, which will eventually

rupture. Dozens to hundreds of these curves can be collected and a histogram of the rupture forces constructed. Reproduced from Bizzarri and Cannistraro[81] with permission from The Royal Society of Chemistry.

While early SMFS experiments were successful in measuring rupture forces and sometimes extrapolating the decay length of the bond[71], real progress in deriving fundamental physicochemical parameters from the system was not made until the arrival of Evans' and Ritchie's landmark 1997 paper[82]. Evans and Ritchie expanded an idea first described by George Bell[83], which offered the insight that the probability of rupture of a bond with energy E_B could be dependent on the force, F, acting upon the bond along the reaction coordinate, x_B:

$$\text{P(bond rupture)} = e^{\frac{-(E_B - Fx_B)}{k_B T}} \qquad \text{Eq. 1}$$

From this, they constructed a model for extracting the energy binding landscape from force spectroscopy experiments. Their understanding that rupture force was linearly dependent on the logarithm of the loading rate (the rate that force is applied to the surface by the probe, equal to the product of the spring constant and the sweep speed of the piezo) allowed for a large number (~100 s) of force-distance curves to be sampled and the number of energy barriers along the path of rupture to be reconstructed (Fig. 8). Description for extracting the off-rate constant (k_{off}) and energy barrier position were incorporated, and the model for force spectroscopy experiments was set for all subsequent work, including the sequential pulling of domains of titin out of the cell membrane[84], serotonin transporter[85], and ricin[72, 86-87]. Further modifications of the model have been made[88] and are still debated, as recent deviations from the 1997 model have been discovered[88]. Furthermore, there remains the practical difficulty of achieving highly rigorous results, with even the original avidin-biotin system showing a range in the literature from 150-350 pN.

$$F^* = \frac{k_B T}{x_\beta} \ln\left(\frac{R x_\beta}{k_{off} k_B T}\right) \qquad \text{Eq. 2}$$

The possibility of the pair rebinding after rupture is nullified by the elastic nature of the molecular linker, which when suitably long, causes the recently ruptured, bound ligand to be pulled well away from the cognate ligand[89].

Another line of inquiry has proceeded, albeit largely theoretically, into determining the Gibbs free energy of these rupture events from force spectroscopy. It may be surprising, at first, that equilibrium quantities such as free energy can be determined from such far-from-equilibrium experiments, but Hummer and Szabo determined[90] that the Jarzynski identity[91] could be applied in such cases, provided that the energy binding landscape was sufficiently sampled. Subsequent work by Liphardt and coworkers successfully applied this to a real-world system of, determining the free energy of RNA stretching within half the thermal energy of theoretical estimates[92].

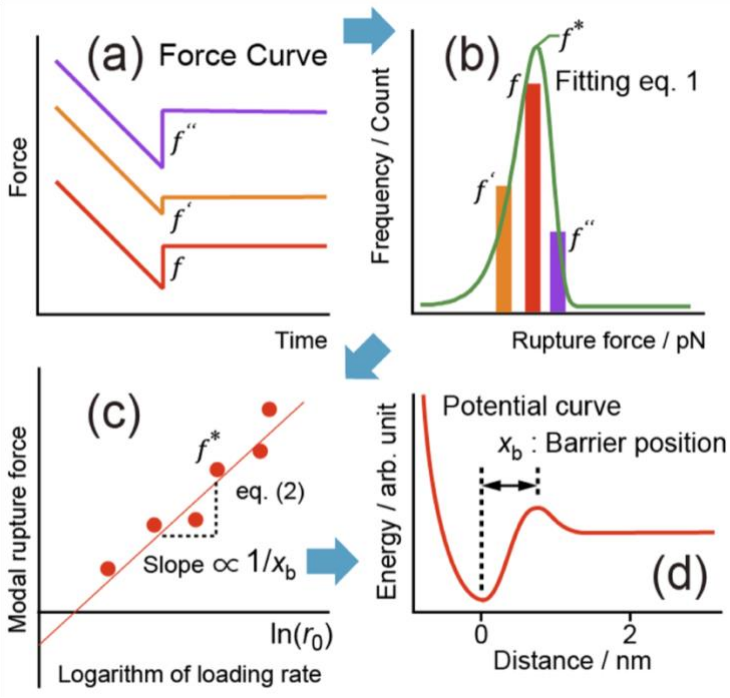

Figure 8. An overview of the application of the Bell-Evans theorem to a SMFS experiment. (a) Many force-distance curves are collected and (b) plotted as a histogram, yielding the most

probable rupture force f* via a Lorentzian fit. (c) Several of these f* values determined at various loading rates can be plotted on a semi-log plot, from which (d) an energy landscape can be derived by Eq. 2. Reproduced under the Creative Commons Attribution license v.3.0 from Taninaka and coworkers[93].

Surface modifications

Because of the small dimensions of molecules, ultraflat gold is necessary to single-molecule experiments. Single crystalline gold (111) surfaces are ideal for this application. Various protocols have been developed to accomplish this: thermal evaporative deposition, plasma vapor deposition, sputter coating, electrochemical deposition, and template stripping of mica or silicon substrates. Thermal evaporation of gold onto mica coupled with high temperature annealing is the simplest, reported in as little as 30 min[94]. It is key that all materials and surfaces be clean. Desorption of all surface-bound water is critical[95] and can be accomplished by heating the surface to several hundred kelvins under high vacuum conditions (where the mean free path is on the order of tens of meters to kilometers).

Mica provides an ideal substrate for AFM experiments due to atomic flatness and hydrophilicity. It is mineral whose structure is comprised of sheets of polymerized silica tetrahedrons cross-linked by cations (commonly aluminum), with coordinating hydroxyl pairs. The sheets are then stuck together with potassium ions. Basal cleavage of the layers is easily achieved, splitting the sheets along the potassium layer, causing potassium ions to be randomly shared between the two newly created layers. This loss of cations gives mica sheets their negative charge.[96]

For the highest possible flatness to be attained, substrate heating is required, wherein the mica sheets sit adjacent to a heating element capable of reaching temperature of 450˚C so that gold

atoms impinging upon the mica surface have sufficient energy to diffuse up to several atomic radii, permitting them to settle into the growing (111) crystal parallel to the mica surface[97]. Lower temperature deposition would create more grain boundaries and thus poorer film quality. Because mica is a high energy charged surface, it will become quickly contaminated outside of vacuum[98]. The presence of potassium ions on the surface when exposed to carbon in the atmosphere can cause the formation of KCO_3 crystals on the surface on the timescale of tens of minutes, degrading flatness, so limiting time between cleavage and implementation of vacuum is necessary.

Tip functionalization

AFM cantilevers are made out of silicon or silicon nitride using standard silicon manufacturing processes. Various methods of functionalization have been developed, including silanization with organofunctional alkoxysilanes[99] and gold-sputtering AFM probes to make them conducive to facile gold-thiol chemistry[100] or click chemistry[101].

Typically, functionalization involves the initial attachment of a bifunctional PEG linker. Commonly, these range from a few to a few dozen nanometers in contour length and are highly flexible (L_p = 0.3 nm), providing the binding pair enough freedom of motion to ensure the unbinding process follows a singular, most energetically favorable path[89]. As the probe moves away, the linker entropically unwinds and exerts force on the binding pair. This force is pivotal in permitting even relatively stiff and slow-responding AFM cantilevers to be used in SMFS experiments[89]. Bifunctionality facilitates tip functionalization, with a thiol or activated ester binding the gold or silanized tip, respectively. The remaining moiety is most commonly a carboxylate, azide, or nitrilotriacetic acid (NTA). Carboxylates can be used to indiscriminately bind exposed primary amines on the ligand via EDC/NHS coupling[102]. Azides can bind alkyne-modified ligands via click chemistry[101], and NTA can bind His_6 site-directed modifications by the

coordination of Ni^{2+} ions[103]. The PEG linker simplifies force spectra interpretation because specific force peaks are expected to occur only around the length of the linker, which allows for algorithmic extraction of peak information. The linker flexibility also increases conformational flexibility of the bound molecule, enabling greater probability that a favorable interaction can be achieved and measured. The elastic nature of the linker serves an additional function of removing the recently unbound ligand away from its receptor so as to reduce the re-binding probability to effectively zero [89].

CHAPTER 2

SINGLE-MOLECULE STUDY OF HEPARIN AND ROBO1

2.1 Introduction

The growing appreciation that GAGs modulate signaling pathways and other biological processes has opened vast new biochemical territory to study. Understanding these processes will enable scientists and physicians a greater ability to control the disease states brought about by GAG-modified pathways, with the ultimate goal of making such pathways amenable to therapies. This thesis demonstrates work done to unite single-molecule methodologies, namely recognition-AFM and AFM-SMFS, to the glycobiological study of the interactions between the Robo1 receptor and the HS analog heparin. This study elucidates the forces involved in the interaction as well as the kinetic parameters, offering a new line of inquiry for this highly interesting pathway.

In order to isolate and interrogate the interactions between heparin (as an HS analog) and Robo1, a model surface was designed and developed. Using a surface-functionalization scheme previously used in our lab[73, 104] based off earlier work with the polysaccharide dextran[105-106], a thermally evaporated gold (111) surface was modified with low-weight, fractionated heparin. This platform presents a controlled surface, with the only interaction observed to be that of the heparin chain. Because it is ultraflat gold (111), it allows for imaging and spectroscopic study of the bound heparin chain without the confounding effects of high baseline surface roughness.

The AFM probe was functionalized to carry the Ig1 and Ig2 ectodomains of the human Robo1 receptor protein (these are the domains of interest that bind Slit[107], and the excision of the transmembrane and cytosolic domains reduces overloading the AFM cantilever without affecting

the overall binding dynamics of the interaction under study). Careful control of the density of PEG linker on the probe via addition of 1-dodecanethiol into the SAM yields a suitably dense linker layer to ensure only one Robo1 protein is experimentally accessible (meaning that only one is in position on the AFM probe to interact with the modified substrate; others may be bound higher up on the tip or even on the cantilever, but because of the length of the linker, these are unable to bind the surface).

TREC imaging and Single-molecule force spectroscopy (SMFS) was carried out on this model surface, successfully probing the physical and kinetic parameters of the binding pair. The nature of single-molecule experiments is inherently statistical, which is discussed, and a series of control experiments were performed to ensure the observed interactions were valid and specific. Challenges with the functionalization protocol are discussed, and a future outlook for this line of inquiry is provided.

2.2 Materials and methods

Materials

Thiol-(polyethylene glycol)-carboxylic acid (MW: 2 kDa) (hereafter referred to as "PEG linker") was purchased from Creative PEGWorks (Chapel Hill, NC, USA). Low-weight, fractionated heparin (MW = 13.5 kDa) was purchased from Scientific Protein Laboratories. Epichlorohydrin was purchased from Acros Organics. Nitric acid was purchased from EMD Millipore. Sodium hydroxide was purchased from BDH. Dimethyl sulfoxide (DMSO) was purchased from Fisher Scientific. Reagent alcohol (comprised of 89-91% ethanol and 4-6% of methanol and 2-propanol) was purchased from VWR. Phosphate buffered saline (pH = 7.2) was prepared from BuPH™ pre-packaged mixtures purchased from Pierce Biotechnology and was filtered through 0.2 μm polytetrafluoroethylene Acrodisc® syringe filters purchased from Pall

Laboratories prior to use as AFM imaging buffer. All other chemicals, hydrochloric acid, N-hydroxysuccinimide (NHS), 11-mercapto-1-undecanol (MUO), 1-(3-dimethylaminopropyl)-3-ethylcarbodimide hydrochloride (EDC), 1-dodecanethiol, and diethylene glycol dimethyl ether (diglyme) were purchased from Sigma-Aldrich. All water was drawn from a core facility Evoqua ultrapure (18MΩ) water system and stored in a polyethylene carboy until use.

Human Robo1 (Ig domains 1 and 2) was obtained from Dr. Lianchun Wang's laboratory, where it was expressed and purified as reported previously[44].

For gold substrates, muscovite mica (grade V1) was purchased form Ted Pella, and 99.999% pure gold pellets were purchased from Kurt Lesker.

For SPM, single-beam cantilever AFM probes with nominal spring constant k_c=0.1 N/m and 10 nm tip radius were purchased from NanoScience Instruments (model number: Aspire CCS-25). STM tips were made form 99.999% gold wire purchased from Alfa Aesar.

Methods

Modification of the gold substrate with heparin

Mica substrates were cut with a guillotine-style paper trimmer to a size of 2 cm x 2 cm so that they would fit into the PTFE liquid cell to undergo modification. In an ISO 5 (Class 100) clean room, these mica pieces were freshly cleaved and placed into a thermal evaporator (Thermionics, Inc.). High vacuum ($<1\times10^{-6}$ torr) was achieved, and the mica substrate was heated to 450˚C at a rate not exceeding 5˚C/minute. After reaching 450˚C, the substrate was left to heat for 1 h before deposition occurred. Gold pellets were melted by passing high current through a molybdenum crucible. Gold was then deposited onto the mica at a rate of 0.3-0.4 Å/s as measured by quartz crystal monitoring until a final thickness of 100 nm was achieved. The substrate was cooled back

to room temperature at a rate never exceeding 8˚C/min, and the substrates were removed from the thermal evaporator and stored under house vacuum for further use (within 2 months).

Immediately prior to use, substrates were annealed for 5 minutes under a hydrogen flame, both to promote the formation of a gold (111) crystalline surface and to remove any contamination. Immediately after annealing, substrates were mounted into the AFM's PTFE liquid cell and 400 µL of 5 mM MUO in DMSO were deposited onto the surface and left to react for 3 h. Excess MUO solution was then removed and the gold surface was rinsed well with reagent alcohol three times followed by three rinses with ultrapure water. Fig. 9 illustrates the process.

Immediately afterward (to avoid possible environmental contamination), a 10 mM epichlorohydrin solution in a 1:1 v/v diglyme and 0.8 M NaOH (aq) is deposited in the liquid cell, covering the gold surface, and left to incubate covered away from light for 4 h. Following this step, the substrate is again rinsed well with reagent alcohol three times and then water three times. Finally, a solution of heparin in water is prepared and deposited in the liquid cell. The sample is then left to react in ambient conditions, for a minimum time of 10 h.

Finally, the sample is rinsed three times with water, and PBS is deposited on the sample until further use.

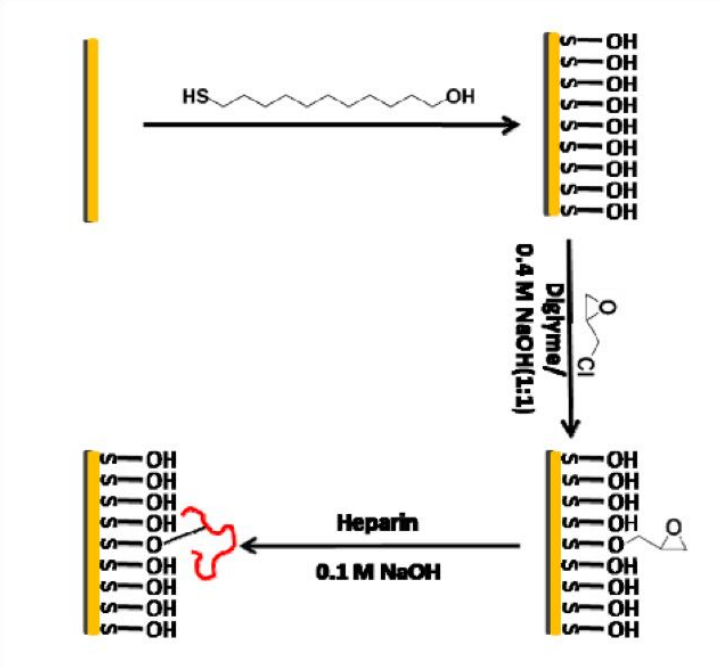

Figure 9. Heparin modification scheme for gold substrates. Gold substrates were prepared according to the above schematic. (A) A SAM of MUO was formed on the gold substrates. (B) Epichlorohydrin was then substituted under basic conditions, followed by (C) incubation with heparin under basic conditions to complete the modification. Reproduced from Guo and coworkers[73] with permission from The Royal Society of Chemistry.

Functionalization of the AFM probe

Silicon single-beam AFM cantilevers (kc = 0.1 N/m) were soaked overnight in a bath of aqua regia (3 parts HCl : 1 part HNO_3 (use caution)) to remove any metal or organic contamination. They were then rinsed three times with ultrapure water and dried in an oven at 200˚C.

The tips were mounted to a sample holder using double-sided Scotch tape with the tip facing down, overhanging the edge of the tape to preclude breaking the cantilever. The backside of the cantilever was then sputter coated in an ion-beam coater (Gatan, Inc.) with a 25 nm layer of nickel

to permit magnetic actuation of the cantilever and to help adhere the following 18 nm layer of gold, deposited to render the cantilever inert and ensure excellent reflectivity of the AFM laser.

The tips were removed from the coater and sample holder and re-mounted with the tip facing up. The tip side was then coated in 5 nm Ni followed by 20 nm Au to permit the attachment of thiolated molecules to the tip. The probes were removed and baked in an oven at 200˚C for 20 min to help ensure the laser spot reflected correctly off of the cantilever. Tips could be stored well-sealed from dust for several months at minimum. Immediately prior to use, tips were cleaned once more by way of a UV/ozone cleaner with the UV lamp active for 15 minutes and then left to sit in the ozone environment for 45 min.

Double-gold-sided tips were immersed in a solution of 0.5 mM HS-PEG-COOH linker and 0.2 mM 1-dodecanethiol in DMSO for 6 h, followed by a thorough rinse in DMSO and then three times rinsed in water. The carboxylic acid moieties on the probes were then converted to active esters with 10 mM EDC NHS, rinsed again in PBS, and then incubated in a solution of Robo1 protein overnight at 4˚C (Fig. 10). Probes were rinsed well in PBS and stored in PBS for use within two days.

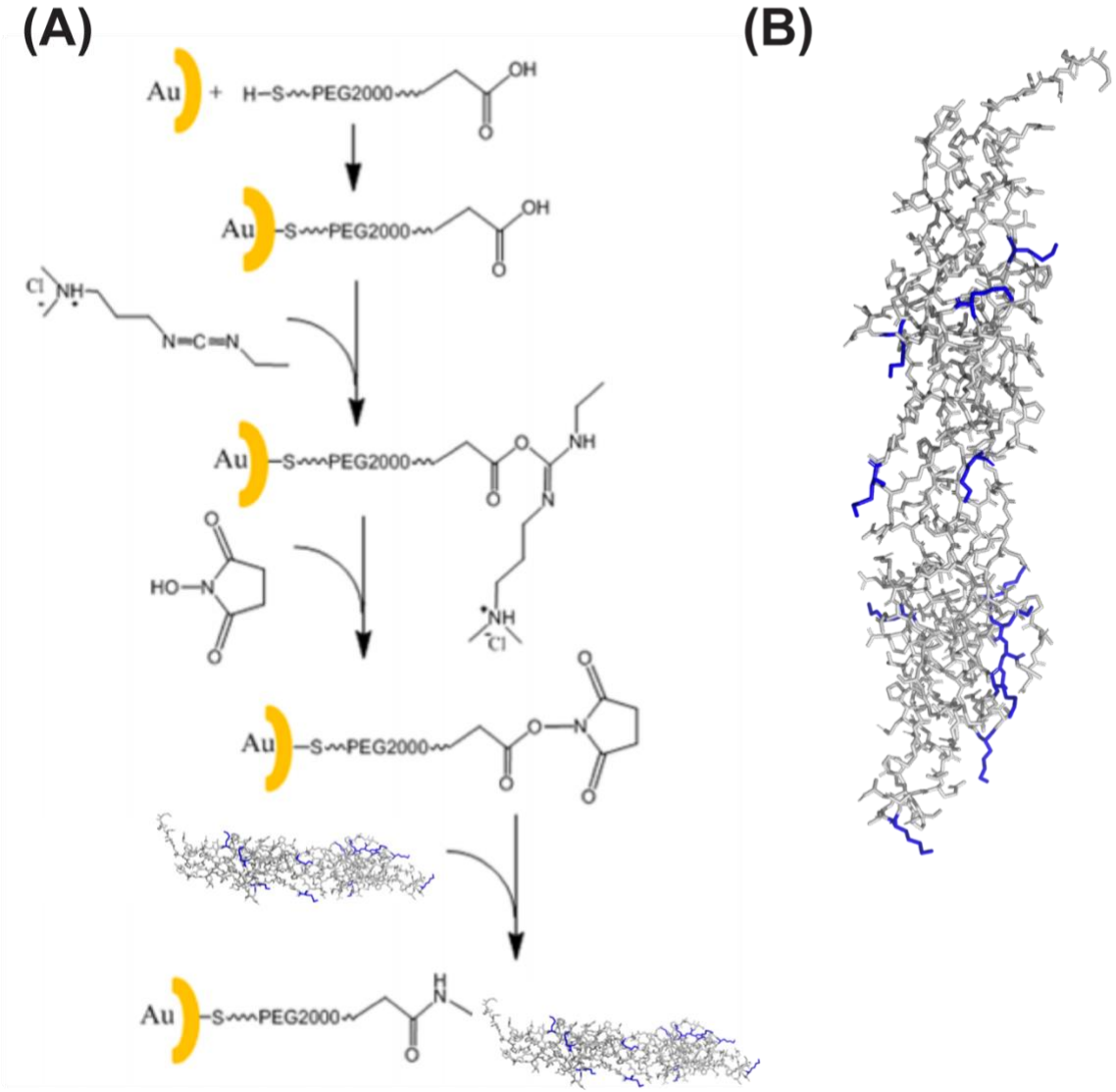

Figure 10. AFM probe functionalization scheme. (A) Gold-coated silicon probes were incubated in a solution of HS–PEG–COOH and 1-dodecanethiol. The acidic functional group was then converted to an active ester by EDC/NHS, followed by prompt addition of the Robo1 peptide, which will covalently attach through its amines. Adapted with permission from Wang and coworkers[72]. (B) Crystal structure of Robo1, with solvent-exposed lysine residues highlighted in blue, rendered in PyMOL, v. 2.2.0 (Schrödinger, LLC) from PDB ID: 2V9Q as determined by Morlot and coworkers[108].

STM imaging

STM images were collected using a Molecular Imaging PicoScan 3000 STM, with the microscope enclosed in a PicoPlus Isolation Chamber to reduce environmental electrical and acoustic noise. The scanner used had a linear pre-amplifier (Keysight, Inc., model N9501A). PicoView v.1.14.4 was used to operate the instrument, and data was processed using Gwyddion v.2.51.

Tips were mechanically cut 99.999% pure gold wire. The instrument was run in constant current mode. To reduce sample damage, imaging was performed with relatively high bias voltages (~0.3-0.5 V) and relatively low set tunneling current (~0.03-0.07 nA).

AFM imaging

An Agilent 5500 AFM (Agilent/Keysight, Chandler, AZ) coupled to an Olympus inverted light microscope, a MAC controller (Agilent/Keysight, Chandler, AZ), and a PicoTREC controller (Agilent/Keysight, Chandler, AZ). Experiments carried out in liquid buffer were done so using a PTFE liquid cell designed for the instrument.

AFM experiments were collected Images were collected using tapping mode AFM with a k_c = 0.102 N/m (measured by thermal tuning) probe magnetically actuated by the scanner (TopMAC) to a free amplitude of ~100 nm. The set point was established to be 85% of the free amplitude as determined by the PicoView software (v1.4). Images were collected at a resolution of 512 × 512 pixels, collected at 1 Hz. The AFM was vibrationally isolated by means of a mechanical vibration pedestal (Minus K Technology).

Force spectroscopy

Functionalized probes were mounted to the AFM and quickly immersed in the imaging buffer in the liquid cell of the sample plate. The system was allowed to equilibrate to ambient

temperatures for at least 30 min prior to beginning to reduce sample drift and temperature-related shifts in the cantilever's resonance frequency.

The AFM probe was actuated under TopMAC mode and lowered into contact with the sample. A TREC image was recorded to establish sample quality, and then the location of the probe was set over one of the gold (111) plateaus commonly observed.

Force-distance curves were collected with a force limit trigger set to 10 mV above the baseline voltage as determined by the PicoView software. Upon hitting the limit, the piezo would retract the AFM probe to reduce the total force applied to the sample and reduce tip wear.

Data analysis

Data analysis proceeded in a hybrid-manner, using a custom-built LabView v.8.6 program to determine the uncoupled unbinding distances and rupture forces. But to couple these distances and forces, the force spectra were analyzed manually. Data was processed using MatLab R2017b (9.3.0).

2.3 Characterization

Heparin-modified substrates were characterized with STM, carried out in ambient conditions. Figure 11 shows this image, along with a control surface that was not modified with heparin. In Figure 11A, three distinct layers are clearly observed. The topographically lowest layer, in black, are pinhole structures in the underlying MUO monolayer. These are caused by underlying defects in the gold substrate and are commonly observed in alkanethiols on gold[97]. The depth of the pinholes here are found to be in agreement with that of other reports of these features, averaging 0.3 nm. While the image fails to resolve individual heparin chain structure, as reported by Guo's and coworkers' seminal paper using this method[73], a distinct layer is observed that, when compared to the control surface, establishes the existence of the heparin layer atop the substrate. Imaging by

Guo was obtained using wax-coated gold tips in PBS, and it is possible that the liquid environment improved the imaging by both reducing any ambient contamination (in practice, surfaces in liquid are less likely to be contaminated by the environment) and possibly by helping shield the charges present on the sulfates, reducing tip-sample interactions and improving the image resolution.

Figure 11C is a model structure of the heparin chain. A characteristic kink is noted, and this is reflected in the STM image. Guo and coworkers were able to resolve the sulfate arms of the heparin chain via STM and found good agreement between their spacing and the distances between the sulfate arms on the model structure.

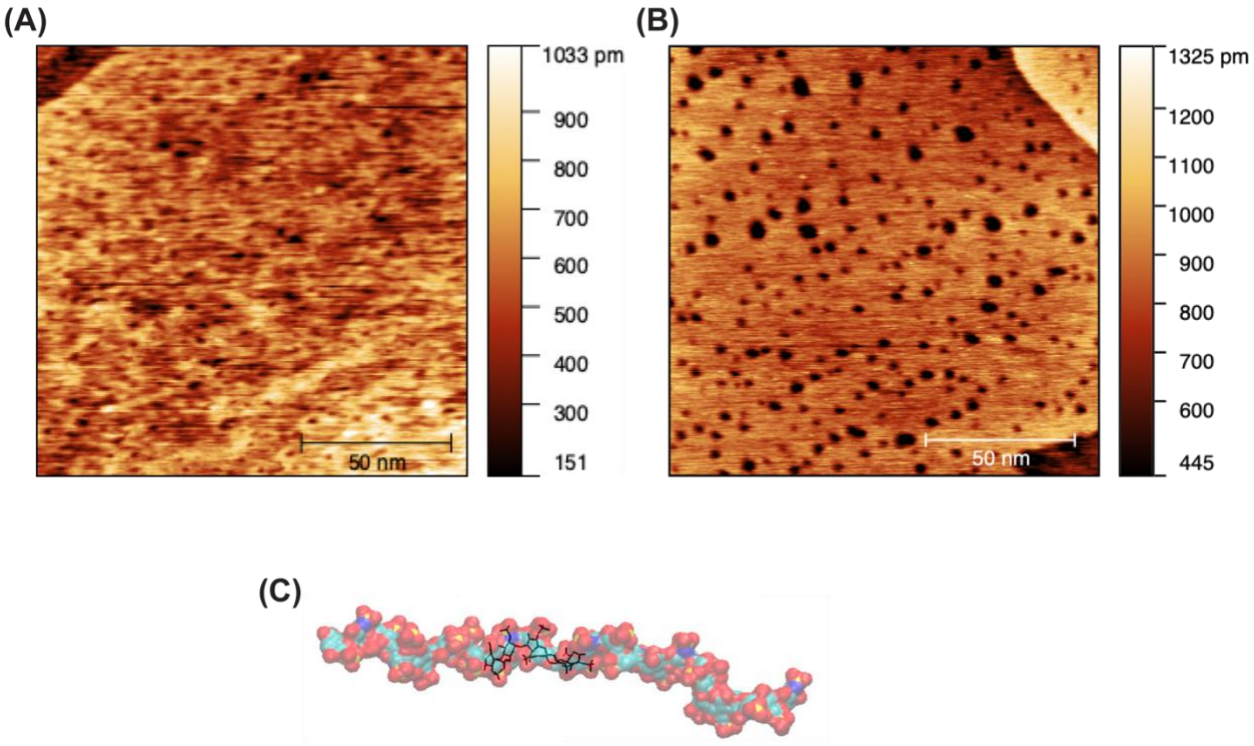

Figure 11. Characterization of the gold substrates. (A) An STM image of heparin-modified gold surface. Three distinctive color ranges are observed: black, corresponding to the pinholes in the underlying MUO SAM; red-orange, corresponding to the MUO monolayer; and yellow-white, corresponding to the attached heparin molecules. For comparison, (B) shows a substrate modified

only with MUO, again showing the pinholes characteristic of alkanethiols on gold, but no additional layer is observed since heparin was never attached. (C) A modeled representation of a heparin chain, showing a characteristic kink near the right end. Structure rendered in PyMol from PDB: 1HPN.

After sample preparation and probe functionalization, topographic, amplitude, and recognition images were recorded with the AFM. The high-quality of the substrate was indicated by the observation of large, flat plateaus of gold (111), containing the step edges intersecting at 60° and 120°, common in crystalline gold (Fig. 12A). Occasional topographic features, typically spots but occasionally filaments on the order of nanometers, were observed, some of which were visualized to be heparin under the recognition image channel (Fig. 12B-C). Because a monolayer of heparin should not prominently present in an AFM topographic image, these are believed to be aggregates of heparin.

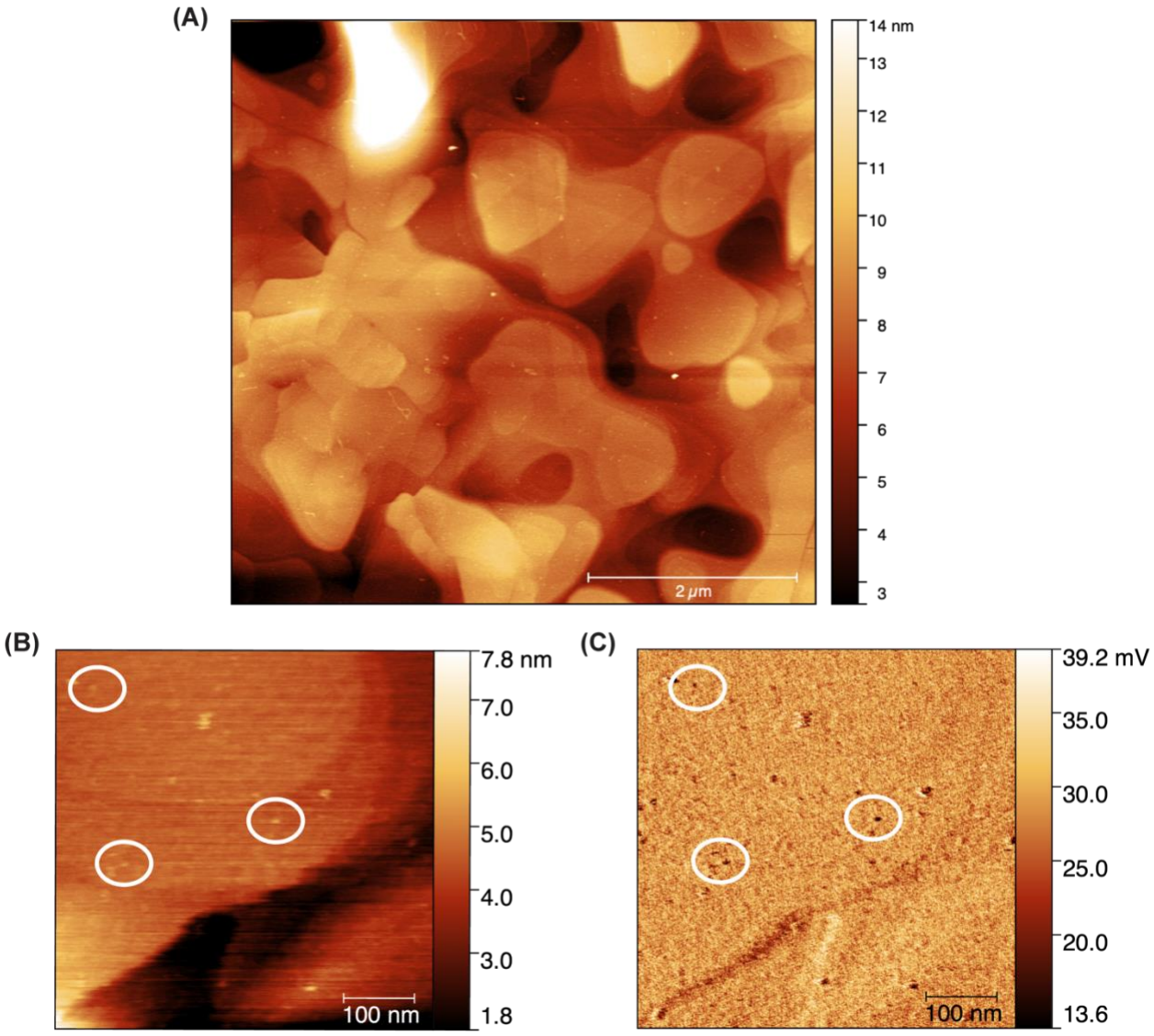

Figure 12. TREC images of the heparin-modified gold surface. (A) A 5 × 5 μm topographic image of the surface shows large, flat plateaus and the triangular step-height patterns common in gold (111) crystal films. (B) A zoomed in image from A shows topographic features, some of which are revealed to be heparin under (C) recognition imaging.

2.4 Single-molecule force spectroscopy

Quantitative information was determined by force spectroscopy. The AFM probe was positioned above a flat region, as determined by TREC imaging, the feedback servo was

deactivated, and the probe was swept into and out of contact with the modified surface at loading rates spanning two orders of magnitude: 1.0, 5.1, 10.2, 30.6, and 102 nN/s. A force peak was determined to be specific when it occurred at an unbinding distance between 5-35 nm (controls confirming this specificity will be discussed later). The PEG linker has a contour length of 15 nm, but its attachment to the conical AFM tip will not necessarily occur at the precise tip apex. Because the collision of the tip apex with the sample establishes the beginning of the contact regime in a force-distance curve, the farther it attaches from the tip apex, the greater the reduction in the apparent binding distance (refer again to Fig. 10 for a schematic). Specific interactions were observed in 41% of these curves, in line with expectations for SMFS experiments. Figure 13A shows that the force peaks do not occur at precisely the same distance for a given probe. This stems from the heparin sugar's slightly lifting off from the gold substrate under the pull of the AFM probe. Because the heparin sugar is anchored to the gold substrate through its hydroxyls in a stochastic manner and the interaction between the relatively structurally homogeneous sugar and Robo1 can occur anywhere along the sugar chain, the AFM probe may pull on the chain at a site along the chain that is not directly anchored to the underlying gold substrate (as seen in the comparison between Fig. 13B and 13C). This allows the chain to lift off the surface slightly prior to the cantilever's exertion of sufficient force to break the intermolecular bonds between the Robo1 peptide and the heparin, and this introduces some tolerance (literally wiggle room) into the observed unbinding distance. The heparin chain is 16.5 nm in length[73], so which gives rise to the 35 nm cutoff mentioned previously. Despite this, the 2D histogram seen in Figure 14 shows that the rupture events are occurring within a narrow band of unbinding distances, and Figure 15 shows the histogram for the rupture forces at each loading rate.

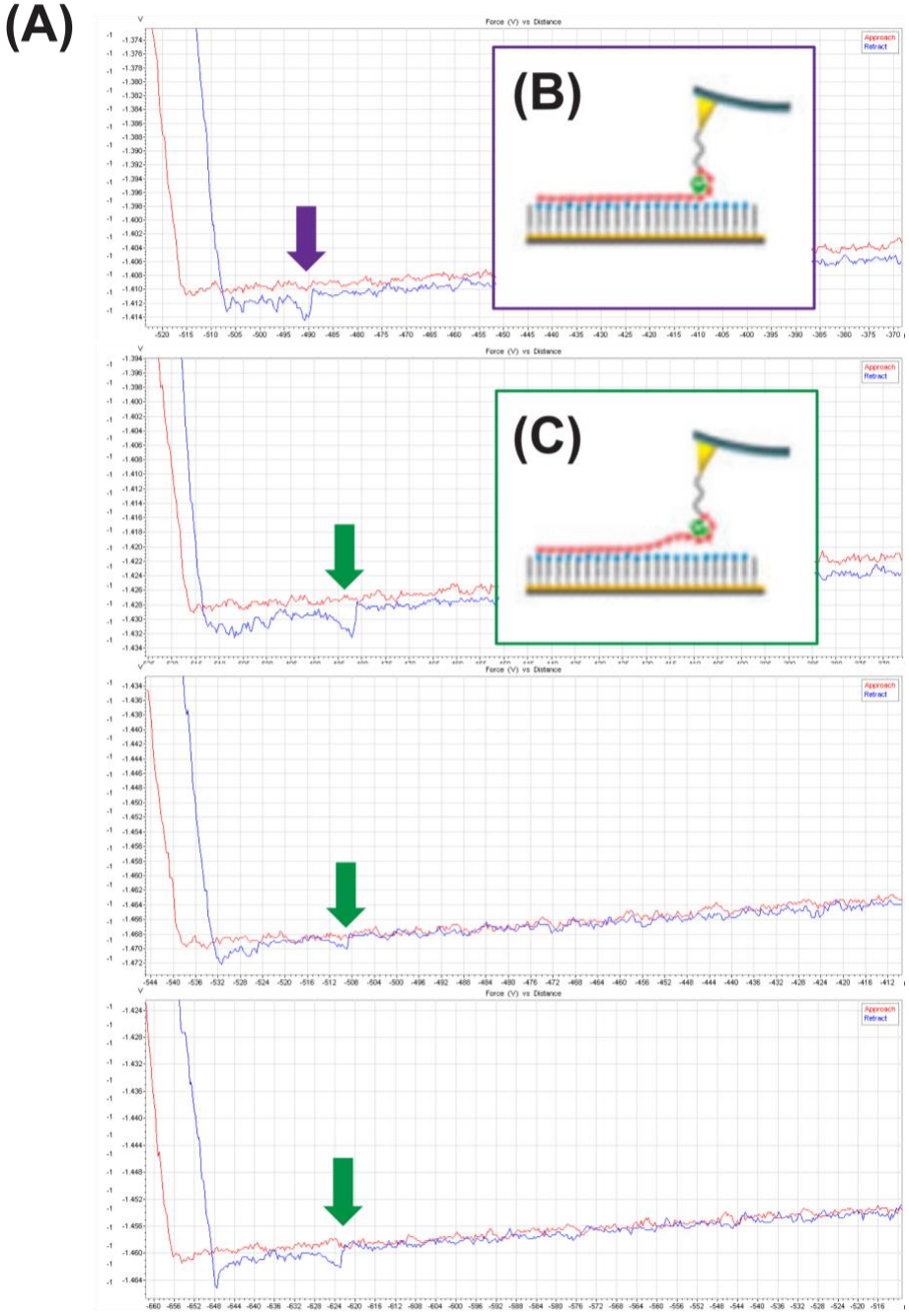

Figure 13. A subset of force-distance curves collected under SMFS. (A) Force-distance curves are shown with the force peak denoted by an arrow. The first force peak (purple arrow) shows up at a shorter rupture length than the other three curves. (B) A cartoon showing a Reproduced from Guo and coworkers[73] with permission from The Royal Society of Chemistry.

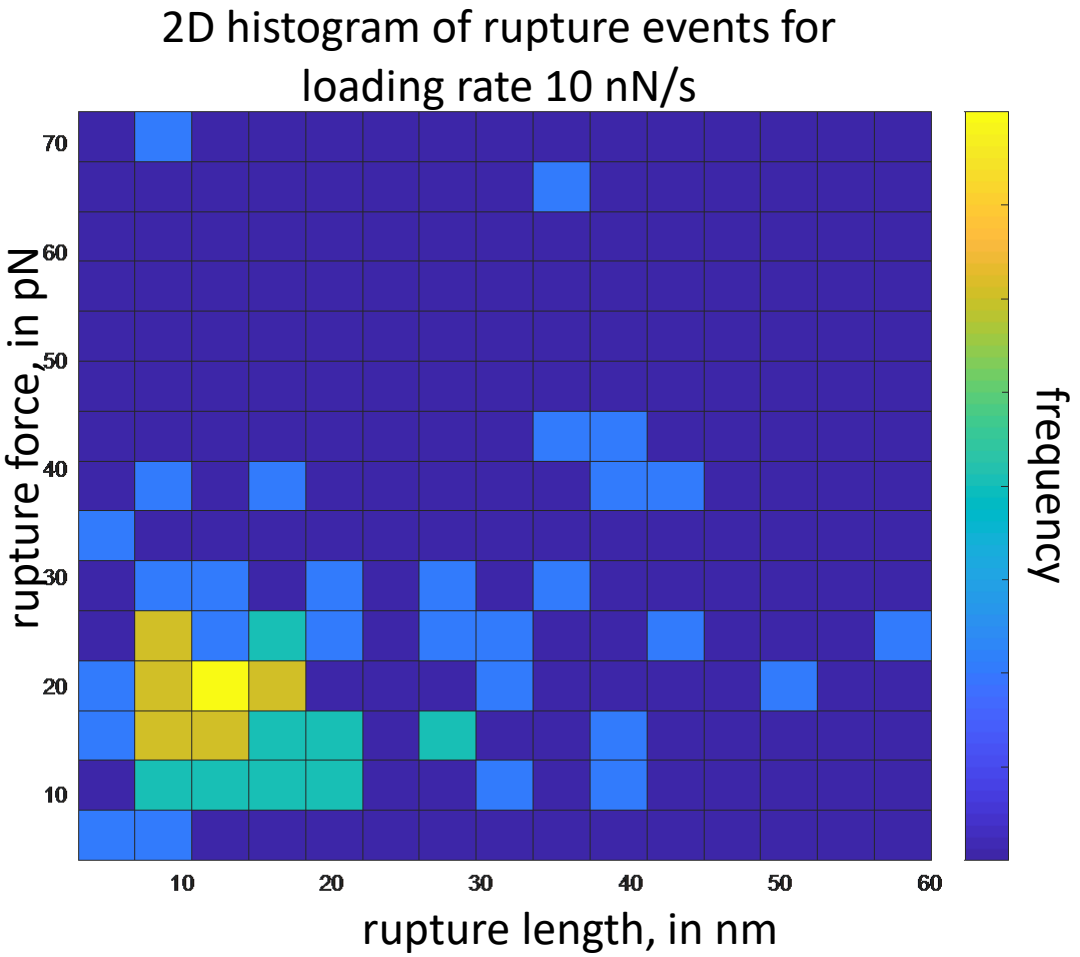

Figure 14. A characteristic two-dimensional histogram showing the distribution of rupture forces and unbinding distances at loading rate 10.2 nN/s.

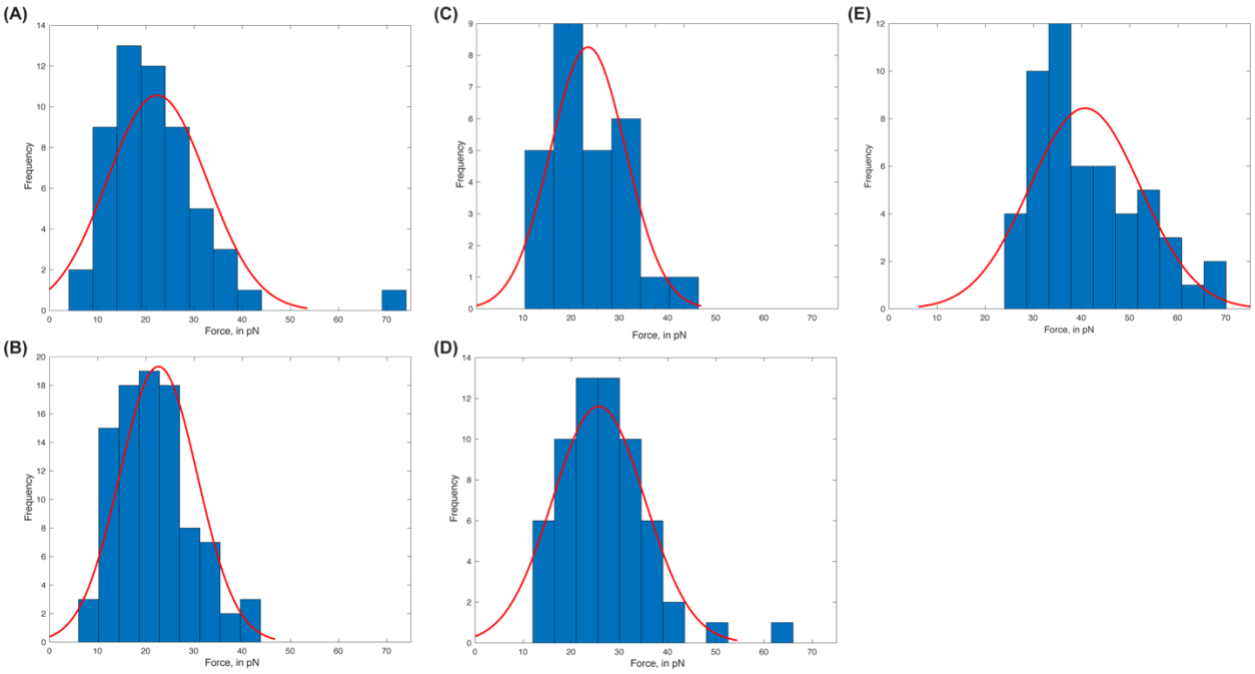

Figure 15. Histograms of rupture forces for loading rates (A) 1.0 nN/s, (B) 5.1 nN/s, (C) 10.2 nN/s, (D) 30.6 nN/s, and (E) 102 nN/s. Overlaid are Gaussian fits for the most probable rupture force.

2.5 Controls and validation

Two control experiments were conducted to ensure the specificity of the observed interaction, a negative control on a gold substrate without heparin, and a blocking experiment where free heparin was introduced into the liquid cell.

In the negative control, the substrate modification scheme was stopped after the SAM of MUO was formed. Force spectroscopy was conducted on this surface at a loading rate of 5.1 nN/s, collecting 100 curves, 8% of which showed a specific interaction, defined as an ostensible rupture peak between 5-30 nm from the tip's departure from the contact regime of the force-distance curve. This was compared to a heparin-modified substrate using the same tip and the same 5.1 nN/s loading rate. This heparin-modified sample showed 41% of curves as having recognition. A z-test for a difference between two proportions was conducted and the observed difference in means

between the heparin-modified and unmodified substrates was found to be highly unlikely to occur by chance under the assumption of no difference between the two samples, with $p = 2.04 \times 10^{-11}$.

A further blocking experiment was conducted to confirm that the Robo1-functionalized tip was binding heparin on the surface and not merely sticking due to some non-specific interaction (Fig. 16). Blocking controls accomplish this through the addition of free ligand into the liquid cell where the force spectroscopy is performed. The free ligand is available to bind the tip-bound receptor, which will occupy the binding site and reduce the probability that the receptor will bind the surface-bound ligand and produce a rupture force peak in the force-distance curve. Force spectra were collected on the heparin-modified surface with the Robo-modified tip, and 46±3.7% of curves (n=186) showed recognition, as defined as above. An aliquot of free aqueous heparin was introduced, increasing the concentration of heparin in the buffer in the liquid cell from 0 to 284 μM. 100 curves were collected, exhibiting 37±4.9% recognition, and an additional aliquot of heparin was introduced, doubling the concentration of heparin to 568 μM, and a further decrease in the probability of interactions to 31.6±3.2% (n=199) was observed. Despite the relatively small amount of heparin added, a significant decrease of interactions is observed (p=0.0015) across the entire experiment.

Considered together, these controls provide strong evidence that the interaction being observed in the force spectra is indeed that between heparin and Robo1.

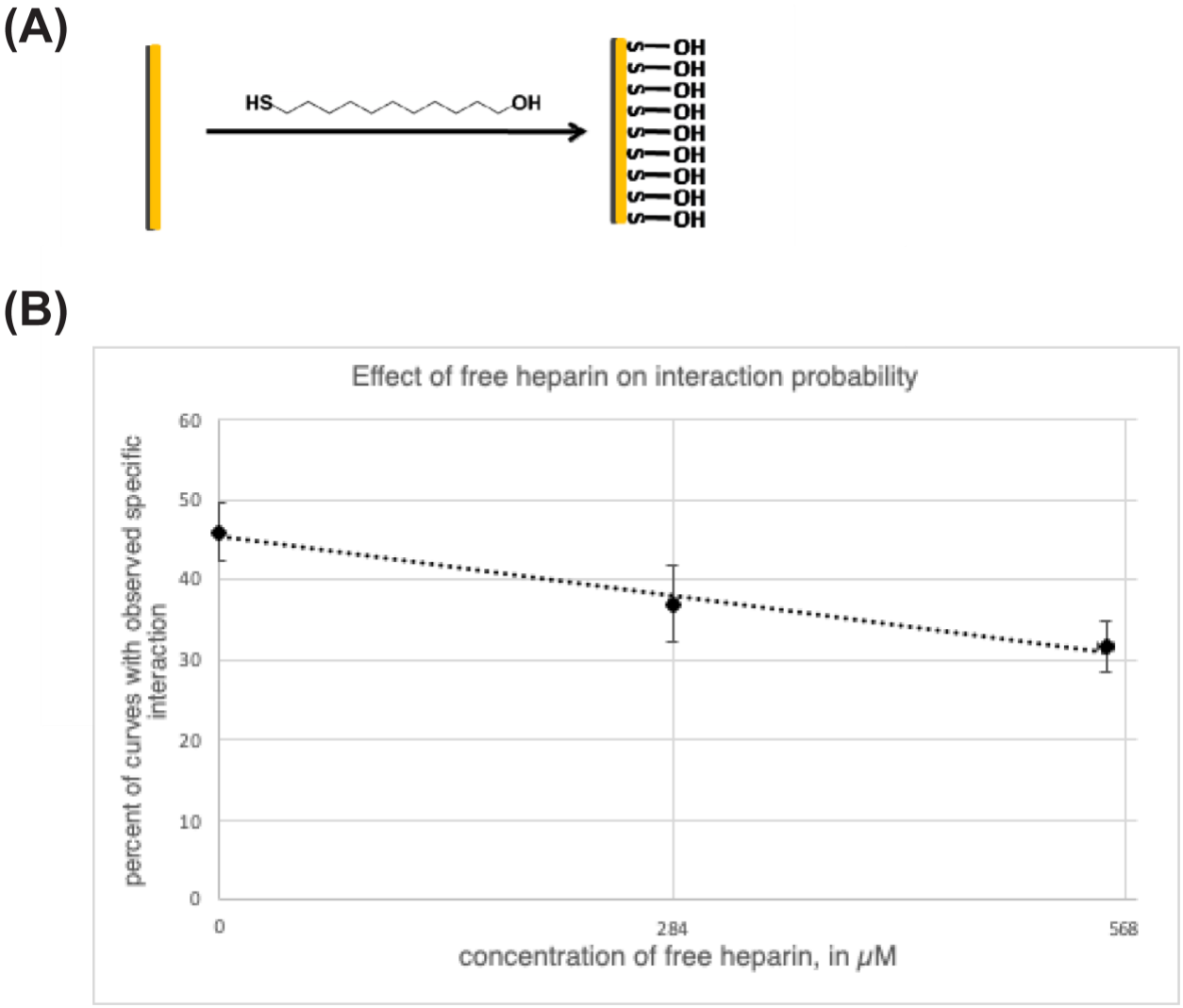

Figure 16. Controls experiments. (A) The scheme for negative controls involves creating a MUO SAM but discontinuing the modification before epichlorohydrin and heparin are added. (B) A plot of the proportion of curves demonstrating interactions as a function of free heparin concentration. Error bars represent standard error.

Another internal quality check on the designed system is necessary to verify that the covalent attachments of the PEG linker, Robo1 protein, MUO SAM, and heparin are all maintain their integrity for the duration of the force spectroscopy experiment. Two qualities ensure this: one is theoretical, the other practical. Each of the covalent bonds involved in the synthesis of the system

is, compared to the non-covalent, intermolecular forces arising at the Robo-heparin interface, extremely strong. Biotin-streptavidin is among the strongest known noncovalent interactions between biological macromolecules, with a most probable rupture force around 350 pN, depending on the loading rate. Covalent bonds rupture at minimum an order of magnitude higher [refs], in the range of nanonewtons or micronewtons. Even accounting for loading rate variation and the Boltzmann distribution, forces this high will effectively never occur in the course of a force spectroscopy experiment.

The other quality check on this process is practical and obvious: the continued observation of force peaks distributed around a mean value of rupture force and occurring within an experimentally expected range of unbinding distance lends further evidence that the molecular functionalization remains present and active. A sudden disappearance of force peaks, or an extreme change in the location or size of the peak could possibly indicate that the system has been damaged or changed (for example, protein denaturation, breakage of the molecular linker, disruption of the modified surface).

2.6 Bell-Evans analysis

The Bell-Evans model was used to interpret the collected curves for kinetic information on the ligand-receptor interactions. A histogram was created for each loading rate collected, and a Gaussian fit of the histogram data established the most probable rupture force, f* (Fig. 15). Figure 16 shows the logarithmic dependence of the observed most probable rupture forces with the loading rate, and a least squares fit of this data produces a good fit. Analysis of the residuals of this fit show that the data point corresponding to 1.0 nN/s loading rate distorts the fit the most, and this can be explained by the thermal and acoustic instability of the AFM over the long operating times required (>6 h) for the collection of spectra at such a low loading rates. A logarithmic regression

is used to fit the data, and despite some non-linearity, a single regression produces the best fit, establishing the presence of a single energy barrier in the unbinding pathway. Correlating the logarithmic regression to the Bell-Evans equation (Eq. 2) allows for the interpretation of the data. Equation 2 can be rewritten as:

$$F^* = \frac{k_B T}{x_\beta} \ln R - \ln\left(\frac{k_{off} k_B T}{x_\beta}\right) \qquad \text{Eq. 3}$$

This allows for facile extraction of x_β and k_{off} from the line of best fit as seen in Fig. 17.

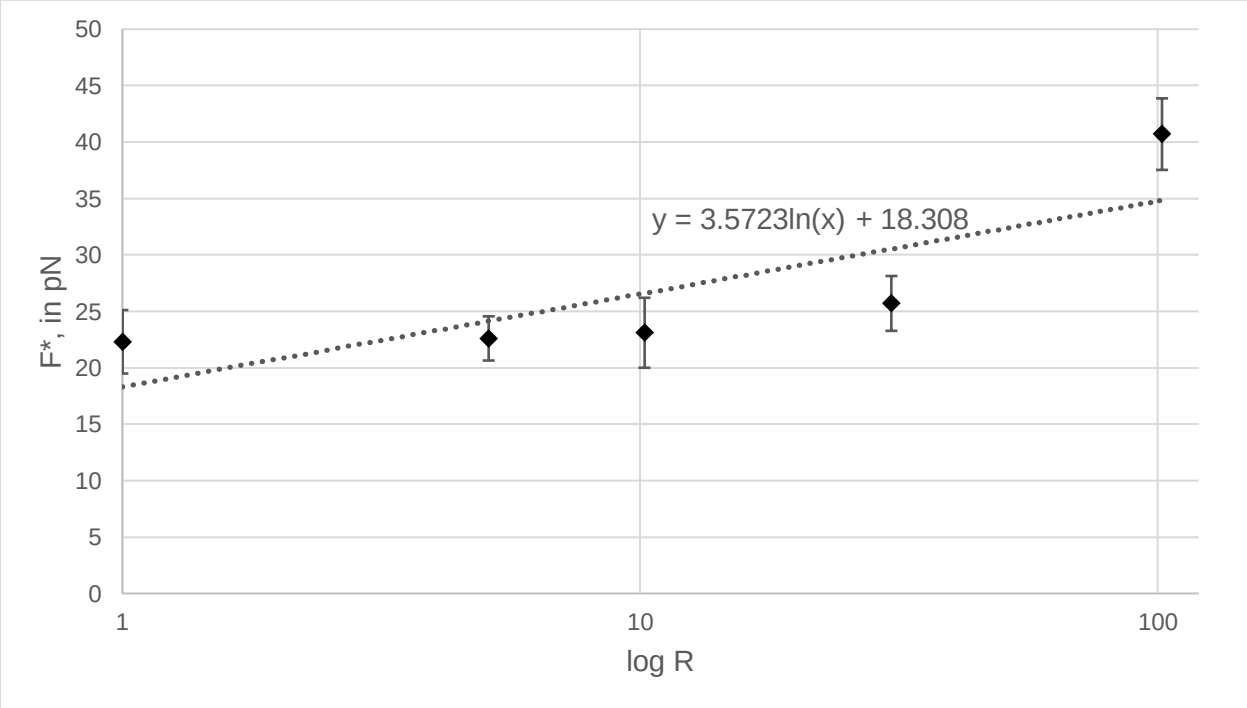

Figure 17. Bell-Evans plot. A semi-log plot showing the most probable rupture force as a function of log (loading rate). The fit line shows the relationship in accordance with the Bell-Evans theorem. Error bars represent the 95% CI.

The experiment occurred at ambient temperature (22°C), so the off-rate constant and energy barrier width are found to be 1.6 s^{-1} and 1.1 nm, respectively. The energy barrier width is high but in otherwise good agreement with similar systems that rely on electrostatic interactions. At first consideration, the off-rate constant appears to be high. But the rapid dissociation of the pair ought

to be interpreted in light of the fact that it is believed that heparin binds Robo solely to stabilize the Slit-Robo complex, not as its primary ligand. This agrees with the observation of the relatively modest diminution of binding probability with increasing free heparin in the blocking control experiment.

CHAPTER 3

CONCLUSIONS AND OUTLOOK

In summary, AFM SMFS has been found to be a useful tool for the interrogation of the interactions between Robo1 and heparin, showing that a specific interaction is occurring at relatively weak yet physiologically relevant interaction strengths. A single energy barrier is determined to separate the bound and unbound states of Robo1-heparin, consistent with the straightforward electrostatic interactions that comprise the interaction. Both the energy barrier width and the off-rate constant were determined by using the Bell-Evans framework used to analyze the force spectroscopy data. The energy barrier width of 1.1 nm is believed to be on the high end of what is possible for electrostatic interactions and may indicate that the relatively open binding pocket and high degree of sulfation allow relatively distant interaction of the ligand-receptor pair. The 1.6 s^{-1} off-rate constant indicates a relatively loose binding state, reflecting the fact that heparin is not Robo's primary ligand but instead a modulating carbohydrate. Moreover, while studies show that specific oligosaccharide sequences are responsible for binding most proteins, including only a tetrasaccharide of heparin for Robo1[107], the full-length of the HS polysaccharide is required for the formation of the ternary complex and further modulation of the interaction is hypothesized to stem from the entire length of the polysaccharide. This work takes advantage of the AFM's ability to use full-length heparin polysaccharides and thus eschews some of the simplifications necessary for other analytical techniques.

Significant challenges were found in the tip functionalization protocol used. These most likely arise out of the choice to use EDC/NHS coupling to bind free primary amines of the Robo1 protein to the AFM probe. The most available sites for this functionalization strategy are lysine residues, but these are implicated in the binding pocket for heparin. This had the effect of rendering ~70% of functionalized tips inactive and unable to observe interactions under force spectroscopy. Development of a more robust functionalize protocol, such as one involving a His_6-tag or a disulfide engineered distal to the binding site would greatly improve experimental efficiency, increasing the number of functionalized AFM probes found to exhibit specific interaction and thus increasing statistical robustness of the collected data.

Future work could reverse the experimental design, attaching HS to the AFM probe via the introduction of a thiol moiety to the end of heparin by reductive amination[109] and Robo1 to the gold surface, indiscriminately bound by EDC/NHS coupling or specifically bound by the introduction of a disulfide or His_6-tag to a region distal to the binding site. Borrowing from an experimental design used previously in the detection of methylation patterns on DNA[110] and lipid-binding domains in prion protein[111], and with prior knowledge of the HS sequence/structure, it would be possible to analyze the unbinding distance of the collected force spectra to determine the oligosaccharide sequence interacting with the surface-bound Robo1 protein, allowing for greater comparison between SMFS-based methods and more mature technologies[41, 43]. TREC imaging would also provide information beyond what is capable with the current methods because the tip's functionalization moiety would be smaller than the receptor on the surface, enabling insight into the structural details of the binding pocket. Additional work could include embedding the receptor in a solid supported lipid bilayer, which would further mimic physiological conditions.

Eventually, this work could be brought to an in vitro design where the unique abilities of AFM would permit the measurement of interactions and kinetic parameters involved in the ternary Slit-Robo-HS complex or its constituent parts at the unparalleled temporal and spatial resolutions inherent to single-molecule methods.

REFERENCES

1. Lim, W.; Mayer, B.; Pawson, T., *Cell Signaling: Principles and Mechanisms*. Garland Science, Taylor & Francis Group: 2014.
2. Hancock, J. T., *Cell Signalling*. Oxford University Press: 2017.
3. Norregaard, K.; Metzler, R.; Ritter, C. M.; Berg-Sørensen, K.; Oddershede, L. B., Manipulation and Motion of Organelles and Single Molecules in Living Cells. *Chemical Reviews* **2017,** *117* (5), 4342-4375.
4. Cho, W.; Stahelin, R. V., Membrane-protein interactions in cell signaling and membrane trafficking. *Annu Rev Biophys Biomol Struct* **2005,** *34*, 119-51.
5. Helm, C. A.; Knoll, W.; Israelachvili, J. N., Measurement of ligand-receptor interactions. *Proceedings of the National Academy of Sciences* **1991,** *88* (18), 8169-8173.
6. Mammen, M.; Choi, S. K.; Whitesides, G. M., Polyvalent Interactions in Biological Systems: Implications for Design and Use of Multivalent Ligands and Inhibitors. *Angew Chem Int Ed Engl* **1998,** *37* (20), 2754-2794.
7. Hunter, C. A.; Anderson, H. L., What is cooperativity? *Angew Chem Int Ed Engl* **2009,** *48* (41), 7488-99.
8. Lazebnik, Y., Can a biologist fix a radio?--Or, what I learned while studying apoptosis. *Cancer Cell* **2002,** *2* (3), 179-82.
9. Werner, E., Meeting Report: The Future and Limits of Systems Biology. *Science Signaling* **2005,** *2005* (278), pe16-pe16.
10. Wang, L.-X.; Davis, B. G., Realizing the Promise of Chemical Glycobiology. *Chem Sci*

2013, *4* (9), 3381-3394.

11. Imperiali, B., The Chemistry–Glycobiology Frontier. *Journal of the American Chemical Society* **2012,** *134* (43), 17835-17839.
12. Dwek, R. A., Glycobiology : Toward Understanding the Function of Sugars. **1996**.
13. Seeberger, P. H., Chemical glycobiology: why now? *Nature Chemical Biology* **2009,** *5*, 368-368.
14. Dube, D. H.; Champasa, K.; Wang, B., Chemical tools to discover and target bacterial glycoproteins the areas of chemical biology. **2011,** (May), 87-101.
15. Buskas, T.; Thompson, P.; Boons, G. J., Immunotherapy for cancer: synthetic carbohydrate-based vaccines. *Chem Commun (Camb)* **2009,** (36), 5335-49.
16. Astronomo, R. D.; Burton, D. R., Carbohydrate vaccines: developing sweet solutions to sticky situations? *Nat Rev Drug Discov* **2010,** *9* (4), 308-24.
17. Bernardi, A.; Jimenez-Barbero, J.; Casnati, A.; De Castro, C.; Darbre, T.; Fieschi, F.; Finne, J.; Funken, H.; Jaeger, K. E.; Lahmann, M.; Lindhorst, T. K.; Marradi, M.; Messner, P.; Molinaro, A.; Murphy, P. V.; Nativi, C.; Oscarson, S.; Penades, S.; Peri, F.; Pieters, R. J.; Renaudet, O.; Reymond, J. L.; Richichi, B.; Rojo, J.; Sansone, F.; Schaffer, C.; Turnbull, W. B.; Velasco-Torrijos, T.; Vidal, S.; Vincent, S.; Wennekes, T.; Zuilhof, H.; Imberty, A., Multivalent glycoconjugates as anti-pathogenic agents. *Chem Soc Rev* **2013,** *42* (11), 4709-27.
18. Seeger, M.; Tear, G.; Ferres-Marco, D.; Goodman, C. S., Mutations affecting growth cone guidance in Drosophila: genes necessary for guidance toward or away from the midline. *Neuron* **1993,** *10* (3), 409-26.
19. Brose, K.; Bland, K. S.; Wang, K. H.; Arnott, D.; Henzel, W.; Goodman, C. S.; Tessier-

Lavigne, M.; Kidd, T., Slit proteins bind Robo receptors and have an evolutionarily conserved role in repulsive axon guidance. *Cell* **1999,** *96* (6), 795-806.

20. Ronca, F.; Andersen, J. S.; Paech, V.; Margolis, R. U., Characterization of Slit protein interactions with glypican-1. *J Biol Chem* **2001,** *276* (31), 29141-7.

21. Hinck, L., The versatile roles of "axon guidance" cues in tissue morphogenesis. 2004; Vol. 7, pp 783-793.

22. Hohenester, E., Structural insight into Slit–Robo signalling. *Biochem. Soc. Trans.* **2008,** *36*, 251-256.

23. Hussain, S.-A. A.; Piper, M.; Fukuhara, N.; Strochlic, L.; Cho, G.; Howitt, J. A.; Ahmed, Y.; Powell, A. K.; Turnbull, J. E.; Holt, C. E.; Hohenester, E., A molecular mechanism for the heparan sulfate dependence of slit-robo signaling. *J. Biol. Chem.* **2006,** *281* (51), 39693-39698.

24. Chiodelli, P.; Bugatti, A.; Urbinati, C.; Rusnati, M., Heparin/Heparan Sulfate Proteoglycans Glycomic Interactome in Angiogenesis: Biological Implications and Therapeutical Use. **2015**, 6342-6388.

25. Fuster, M. M.; Wang, L., Endothelial Heparan Sulfate in Angiogenesis I . Endothelial Heparan Sulfate in Developmental and Physiologic Angiogenesis A . Angiogenesis in Health and Disease : An Introduction. 2010; Vol. 93, pp 179-212.

26. Chédotal, A.; Kerjan, G.; C, M.-F., The brain within the tumor: new roles for axon guidance molecules in cancers. *Cell Death Differ* **2005,** *12* (8), 1044-1056.

27. Zhao, J.; Mommersteeg, M. T. M., Slit-Robo signalling in heart development. *Cardiovascular Research* **2018,** *114* (6), 794-804.

28. Blockus, H.; Chédotal, A., The multifaceted roles of Slits and Robos in cortical circuits:

From proliferation to axon guidance and neurological diseases. *Curr Opin Neurobiol* **2014,** *27*, 82-88.

29. Sasisekharan, R.; Venkataraman, G., Heparin and heparan sulfate : biosynthesis , structure and function. *Current Opinion in Chemical Biology* **2000,** *4*, 626-631.

30. Inatani, M.; Irie, F.; Plump, A. S.; Tessier-Lavigne, M.; Yamaguchi, Y., Mammalian brain morphogenesis and midline axon guidance require heparan sulfate. *Science* **2003,** *302* (5647), 1044-6.

31. Sarrazin, S.; Lamanna, W. C.; Esko, J. D., Heparan sulfate proteoglycans. *Cold Spring Harb Perspect Biol* **2011,** *3* (7).

32. Bülow, H. E.; Hobert, O., The Molecular Diversity of Glycosaminoglycans Shapes Animal Development. *Annual Review of Cell and Developmental Biology* **2006,** *22* (1), 375-407.

33. Steigemann, P.; Molitor, A.; Fellert, S.; Jäckle, H.; Vorbrüggen, G., Heparan Sulfate Proteoglycan Syndecan Promotes Axonal and Myotube Guidance by Slit/Robo Signaling. *Current Biology* **2004,** *14* (3), 225-230.

34. Warttinger, U.; Giese, C.; Harenberg, J.; Holmer, E.; Krämer, R., A fluorescent probe assay (Heparin Red) for direct detection of heparins in human plasma. *Analytical and Bioanalytical Chemistry* **2016,** *408* (28), 8241-8251.

35. Arungundram, S.; Al-Mafraji, K.; Asong, J.; Leach, F. E.; Amster, I. J.; Venot, A.; Turnbull, J. E.; Boons, G.-J., Modular Synthesis of Heparan Sulfate Oligosaccharides for Structure−Activity Relationship Studies. *Journal of the American Chemical Society* **2009,** *131* (47), 17394-17405.

36. Osmond, R. I. W.; Kett, W. C.; Skett, S. E.; Coombe, D. R., Protein-heparin interactions

measured by BIAcore 2000 are affected by the method of heparin immobilization. *Analytical Biochemistry* **2002,** *310* (2), 199-207.

37. Bertozzi, C. R.; Kiessling, L. L., Chemical Glycobiology. **2001,** *291* (March), 2357-2365.

38. Krishnamoorthy, L.; Mahal, L. K., R EVIEW. **2009,** *4* (9), 715-732.

39. *Essentials of Glycobiology*. 2nd ed.; Cold Spring Harbor Laboratory Press: New York, 2009.

40. Duus, J.; Gotfredsen, C. H.; Bock, K., Carbohydrate structural determination by {NMR} spectroscopy: modern methods and limitations. *Chem. Rev.* **2000,** *100* (12), 4589-4614.

41. Zong, C.; Huang, R.; Condac, E.; Chiu, Y.; Xiao, W.; Li, X.; Lu, W.; Ishihara, M.; Wang, S.; Ramiah, A.; Stickney, M.; Azadi, P.; Amster, J. I.; Moremen, K. W.; Wang, L.; Sharp, J. S.; Boons, G.-J. J.; Amster, I. J.; Moremen, K. W.; Wang, L.; Sharp, J. S.; Boons, G.-J. J., Integrated Approach to Identify Heparan Sulfate Ligand Requirements of Robo1. *Journal of the American Chemical Society* **2016,** *138* (39), 13059-13067.

42. Zaia, J., Glycosaminoglycan Glycomics Using Mass Spectrometry. *Molecular & Cellular Proteomics* **2013,** *12* (4), 885-892.

43. Gao, Q.; Chen, C. Y.; Zong, C.; Wang, S.; Ramiah, A.; Prabhakar, P.; Morris, L. C.; Boons, G. J.; Moremen, K. W.; Prestegard, J. H., Structural aspects of heparan sulfate binding to Robo1-Ig1-2. *ACS Chemical Biology* **2016,** *11* (11), 3106-3113.

44. Zhang, F.; Moniz, H. A.; Walcott, B.; Moremen, K. W.; Linhardt, R. J.; Wang, L., Biochimie Characterization of the interaction between Robo1 and heparin and other glycosaminoglycans. *Biochimie* **2013,** *95* (12), 2345-2353.

45. Lakshminarayanan, A.; Richard, M.; Davis, B. G., Studying glycobiology at the. **2018**.

46. Kitov, P. I.; Bundle, D. R., On the nature of the multivalency effect: a thermodynamic

model. *J Am Chem Soc* **2003,** *125* (52), 16271-84.

47. Mulder, A.; Huskens, J.; Reinhoudt, D. N., Multivalency in supramolecular chemistry and nanofabrication. *Org Biomol Chem* **2004,** *2* (23), 3409-24.

48. Rust, M. J.; Bates, M.; Zhuang, X., Sub-diffraction-limit imaging by stochastic optical reconstruction microscopy (STORM). *Nat Methods* **2006,** *3* (10), 793-5.

49. Betzig, E.; Patterson, G. H.; Sougrat, R.; Lindwasser, O. W.; Olenych, S.; Bonifacino, J. S.; Davidson, M. W.; Lippincott-Schwartz, J.; Hess, H. F., Imaging Intracellular Fluorescent Proteins at Nanometer Resolution. *Science* **2006,** *313* (5793), 1642.

50. Wang, M. D.; Schnitzer, M. J.; Yin, H.; Landick, R.; Gelles, J.; Block, S. M., Force and velocity measured for single molecules of RNA polymerase. *Science* **1998,** *282* (5390), 902-7.

51. Abbondanzieri, E. A.; Greenleaf, W. J.; Shaevitz, J. W.; Landick, R.; Block, S. M., Direct observation of base-pair stepping by RNA polymerase. *Nature* **2005,** *438* (7067), 460-5.

52. Wen, J. D.; Lancaster, L.; Hodges, C.; Zeri, A. C.; Yoshimura, S. H.; Noller, H. F.; Bustamante, C.; Tinoco, I., Following translation by single ribosomes one codon at a time. *Nature* **2008,** *452* (7187), 598-603.

53. Tinoco, I., Jr.; Gonzalez, R. L., Jr., Biological mechanisms, one molecule at a time. *Genes Dev* **2011,** *25* (12), 1205-31.

54. Martines, E.; Zhong, J.; Muzard, J.; Lee, A. C.; Akhremitchev, B. B.; Suter, D. M.; Lee, G. U., Single-molecule force spectroscopy of the aplysia cell adhesion molecule reveals two homophilic bonds. *Biophysical Journal* **2012,** *103* (4), 649-657.

55. Wang, B.; Lou, Z.; Park, B.; Kwon, Y.; Zhang, H.; Xu, B., Surface conformations of an anti-ricin aptamer and its affinity for ricin determined by atomic force microscopy and

surface plasmon resonance. *Phys. Chem. Chem. Phys.* **2015,** *17* (1), 307-314.

56. Binnig, G.; Rohrer, H.; Gerber, C.; Weibel, E., Vacuum tunneling. *Physica B+C* **1982**.

57. Binnig, G.; Quate, C. F.; Gerber, C., Atomic Force Microscope. *Phys Rev Lett* **1986,** *56* (9), 930-930.

58. Meyer, G.; Amer, N. M., Novel optical approach to atomic force microscopy. *Applied Physics Letters* **1988,** *53* (12), 1045-1047.

59. Zhong, Q.; Inniss, D.; Kjoller, K.; Elings, V. B., Fractured polymer/silica fiber surface studied by tapping mode atomic force microscopy. *Surface Science Letters* **1993,** *290* (1-2), L688-L692.

60. Drake, B.; Prater, C. B.; Weisenhorn, A. L.; Gould, S. A. C.; Albrecht, T. R.; Quate, C. F.; Cannell, D. S.; Hansma, H. G.; Hansma, P. K., Imaging crystals, polymers, and processes in water with the atomic force microscope. *Science* **1989,** *243* (4898), 1586-1589.

61. Ebner, A.; Hinterdorfer, P.; Gruber, H. J., Comparison of different aminofunctionalization strategies for attachment of single antibodies to AFM cantilevers. *Ultramicroscopy* **2007,** *107* (10-11), 922-927.

62. Ebner, A.; Kienberger, F.; Kada, G.; Stroh, C. M.; Geretschläger, M.; Kamruzzahan, A. S. M.; Wildling, L.; Johnson, W. T.; Ashcroft, B.; Nelson, J.; Lindsay, S. M.; Gruber, H. J.; Hinterdorfer, P., Localization of single Avidin-Biotin interactions using simultaneous topography and molecular recognition imaging. *ChemPhysChem* **2005,** *6* (5), 897-900.

63. Li, Q.; Zhang, T.; Pan, Y.; Ciacchi, L. C.; Xu, B.; Wei, G., AFM-based force spectroscopy for bioimaging and biosensing. *RSC Adv.* **2016,** *6* (16), 12893-12912.

64. Alexander Reese, R.; Xu, B., Single-molecule detection of proteins and toxins in food

using atomic force microscopy. *Trends in Food Science and Technology* **2019,** *83* (September 2017), 277-284.

65. Fotiadis, D.; Muller, D. J.; Tsiotis, G.; Hasler, L.; Tittmann, P.; Mini, T.; Jeno, P.; Gross, H.; Engel, A., Surface analysis of the photosystem I complex by electron and atomic force microscopy. *J Mol Biol* **1998,** *283* (1), 83-94.

66. Oteyza, D. G. d.; Gorman, P.; Chen, Y.-C.; Wickenburg, S.; Riss, A.; Mowbray, D. J.; Etkin, G.; Pedramrazi, Z.; Tsai, H.-Z.; Rubio, A.; Crommie, M. F.; Fischer, F. R., Direct Imaging of Covalent Bond Structure in Signle-Molecule Chemical Reactions. *Science* **2013,** *340* (6139), 1434-1437.

67. Giessibl, F. J., AFM's path to atomic resolution. *Materials Today* **2005,** *8* (5), 32-41.

68. Gross, L.; Mohn, F.; Moll, N.; Liljeroth, P.; Meyer, G., The chemical structure of a molecule resolved by atomic force microscopy. *Science* **2009,** *325* (5944), 1110-4.

69. Israelachvili, J. N., *Intermolecular and Surface Forces*. 3rd ed.; Academic Press: 2011; p 704.

70. Müller, D. J.; Fotiadis, D.; Scheuring, S.; Müller, S. A.; Engel, A., Electrostatically balanced subnanometer imaging of biological specimens by atomic force microscope. *Biophysical Journal* **1999,** *76* (2), 1101-1111.

71. Florin, E. L.; Moy, V. T.; Gaub, H. E., Adhesion forces between individual ligand-receptor pairs. *Science* **1994,** *264* (5157), 415-417.

72. Wang, B.; Guo, C.; Chen, G.; Park, B.; Xu, B., Following aptamer-ricin specific binding by single molecule recognition and force spectroscopy measurements. *Chemical Communications* **2012,** *48* (11), 1644-1646.

73. Guo, C.; Wang, B.; Wang, L.; Xu, B., Structural Basis of Single Molecular Heparin-

FX06 Interaction Revealed by SPM Measurements and Molecular Simulations. *Chemical Communications* **2012,** *3* (100), 12222-12224.

74. Zlatanova, J.; Lindsay, S. M.; Leuba, S. H., Single molecule force spectroscopy in biology using the atomic force microscope. *Progress in Biophysics & Molecular Biology* **2000,** *74*, 37-61.

75. Moreno-Herrero, F.; Herrero, P.; Colchero, J.; Baró, A. M.; Moreno, F., Imaging and Mapping Protein-Binding Sites on DNA Regulatory Regions with Atomic Force Microscopy. *Biochemical and Biophysical Research Communications* **2001,** *280* (1), 151-157.

76. Ando, T.; Uchihashi, T.; Fukuma, T., High-speed atomic force microscopy for nano-visualization of dynamic biomolecular processes. *Progress in Surface Science* **2008,** *83* (7), 337-437.

77. Kodera, N.; Yamamoto, D.; Ishikawa, R.; Ando, T., Video imaging of walking myosin V by high-speed atomic force microscopy. *Nature* **2010,** *468* (7320), 72-6.

78. Igarashi, K.; Uchihashi, T.; Koivula, A.; Wada, M.; Kimura, S.; Okamoto, T.; Penttila, M.; Ando, T.; Samejima, M., Traffic jams reduce hydrolytic efficiency of cellulase on cellulose surface. *Science* **2011,** *333* (6047), 1279-82.

79. Uchihashi, T.; Iino, R.; Ando, T.; Noji, H., High-speed atomic force microscopy reveals rotary catalysis of rotorless F(1)-ATPase. *Science* **2011,** *333* (6043), 755-8.

80. Shibata, M.; Nishimasu, H.; Kodera, N.; Hirano, S.; Ando, T.; Uchihashi, T.; Nureki, O., Real-space and real-time dynamics of CRISPR-Cas9 visualized by high-speed atomic force microscopy. *Nat Commun* **2017,** *8* (1), 1430.

81. Bizzarri, A. R.; Cannistraro, S., The application of atomic force spectroscopy to the study

of biological complexes undergoing a biorecognition process. *Chemical Society Reviews* **2010,** *39* (2), 734-749.

82. Evans, E.; Ritchie, K., Dynamic strength of molecular adhesion bonds. *Biophysical Journal* **1997,** *72* (4), 1541-1555.

83. Bell, G. I., Models for the specific adhesion of cells to cells. *Science* **1978,** *200* (4342), 618-627.

84. Oberhauser, A. F.; Hansma, P. K.; Carrion-Vazquez, M.; Fernandez, J. M., Stepwise unfolding of titin under force-clamp atomic force microscopy. *Proceedings of the National Academy of Sciences* **2001,** *98* (2), 468-472.

85. Wildling, L.; Rankl, C.; Haselgrübler, T.; Gruber, H. J.; Holy, M.; Newman, A. H.; Zou, M.-F.; Zhu, R.; Freissmuth, M.; Sitte, H. H.; Hinterdorfer, P., Probing Binding Pocket of Serotonin Transporter by Single Molecular Force Spectroscopy on Living Cells. *Journal of Biological Chemistry* **2011,** *287* (1), 105-113.

86. Chen, G.; Zhou, J.; Park, B.; Xu, B., Single ricin detection by atomic force microscopy chemomechanical mapping. *Applied Physics Letters* **2009,** *95* (4), 043103-043103.

87. Wang, B.; Guo, C.; Zhang, M.; Park, B.; Xu, B., High-Resolution Single-Molecule Recognition Imaging of the Molecular Details of Ricin–Aptamer Interaction. *The Journal of Physical Chemistry B* **2012,** *116* (17), 5316-5322.

88. Hane, F. T.; Attwood, S. J.; Leonenko, Z., Comparison of three competing dynamic force spectroscopy models to study binding forces of amyloid-beta (1-42). *Soft Matter* **2014,** *10* (12), 1924-30.

89. Takeuchi, O.; Miyakoshi, T.; Taninaka, A.; Tanaka, K.; Cho, D.; Fujita, M.; Yasuda, S.; Jarvis, S. P.; Shigekawa, H., Dynamic-force spectroscopy measurement with precise

force control using atomic-force microscopy probe. *Journal of Applied Physics* **2006,** *100* (7).

90. Hummer, G.; Szabo, A., Free energy reconstruction from nonequilibrium single-molecule pulling experiments. *Proceedings of the National Academy of Sciences* **2001,** *98* (7), 3658-3661.

91. Jarzynski, C., Nonequilibrium Equality for Free Energy Differences. *Physical Review Letters* **1997,** *78* (14), 2690-2693.

92. Liphardt, J.; Dumont, S.; Smith, S. B.; Tinoco, I., Jr.; Bustamante, C., Equilibrium Information from Nonequilibrium Measurements in an Experimental Test of Jarzynski's Equality. *Science* **2002,** *296* (5574), 1832-1835.

93. Taninaka, A.; Hirano, Y.; Takeuchi, O.; Shigekawa, H., Force measurement enabling precise analysis by dynamic force spectroscopy. *Int J Mol Sci* **2012,** *13* (1), 453-65.

94. Nogues, C.; Wanunu, M., A rapid approach to reproducible, atomically flat gold films on mica. *Surface Science* **2004,** *573* (3).

95. Klein, H.; Blanc, W.; Pierrisnard, R.; Fauquet, C.; Dumas, P., Self-assembled monolayers of decanethiol on Au(111)/mica. *European Physical Journal B* **2000,** *14* (2), 371-376.

96. Lyubchenko, Y. L.; Shlyakhtenko, L. S., Imaging of DNA and Protein-DNA Complexes with Atomic Force Microscopy. *Critical Reviews in Eukaryotic Gene Expression* **2016,** *26* (1), 63-96.

97. Guo, L. H.; Facci, J. S.; McLendon, G.; Mosher, R., Effect of Gold Topography and Surface Pretreatment on the Self-Assembly of Alkanethiol Monolayers. *Langmuir* **1994,** *10* (12), 4588-4593.

98. Israelachvili, J. N.; Alcantar, N. A.; Maeda, N.; Mates, T. E.; Ruths, M., Preparing

contamination-free mica substrates for surface characterization, force measurements, and imaging. *Langmuir* **2004,** *20* (9), 3616-3622.

99. Kudera, M.; Eschbaumer, C.; Gaub, H. E.; Schubert, U. S., Analysis of metallo-supramolecular systems using single-molecule force spectroscopy. *Advanced Functional Materials* **2003,** *13* (8), 615-620.

100. Guo, C.; Fan, X.; Qiu, H.; Xiao, W.; Wang, L.; Xu, B., High-resolution probing heparan sulfate-antithrombin interaction on a single endothelial cell surface: Single-molecule AFM studies. *Physical Chemistry Chemical Physics* **2015,** *17* (20), 13301-13306.

101. Chen, G.; Ning, X.; Park, B.; Boons, G.-J.; Xu, B., Simple, Clickable Protocol for Atomic Force Microscopy Tip Modification and Its Application for Trace Ricin Detection by Recognition Imaging. *Langmuir* **2009,** *25* (5), 2860-2864.

102. Haselgrübler, T.; Amerstorfer, A.; Schindler, H.; Gruber, H. J., Synthesis and applications of a new poly(ethylene glycol) derivative for the crosslinking of amines with thiols. *Bioconjugate Chemistry* **1995,** *6*, 242-248.

103. Verbelen, C.; Gruber, H. J.; Dufrene, Y. F., The NTA-His6 bond is strong enough for AFM single-molecular recognition studies. *Journal of Molecular Recognition* **2007,** *20* (6), 490-4.

104. Zhang, T. The Role of Heparin in the Prion Proteins Aggregation. University of Georgia, Athens, GA, 2017.

105. Alquist, F. N.; Slagh, H. R. Ethers of chlorophenols. 1940.

106. Löfås, S., Dextran modified self-assembled monolayer surfaces for use in biointeraction analysis with surface plasmon resonance. *Pure and Applied Chemistry* **1995,** *67* (5), 829-834.

107. Fukuhara, N.; Howitt, J. A.; Hussain, S.-a.; Hohenester, E., Structural and Functional Analysis of Slit and Heparin Binding to Immunoglobulin-like Domains 1 and 2 of Drosophila Robo *. **2008,** *283* (23), 16226-16234.

108. Morlot, C.; Thielens, N. M.; Ravelli, R. B. G.; Hemrika, W.; Romijn, R. A.; Gros, P.; Cusack, S.; McCarthy, A. A., Structural insights into the Slit-Robo complex. *Proceedings of the National Academy of Sciences of the United States of America* **2007,** *104* (38), 14923-14928.

109. Lee, K.; Lee, H.; Bae, K. H.; Park, T. G., Heparin immobilized gold nanoparticles for targeted detection and apoptotic death of metastatic cancer cells. *Biomaterials* **2010,** *31* (25), 6530-6536.

110. Zhu, R.; Howorka, S.; Pröll, J.; Kienberger, F.; Preiner, J.; Hesse, J.; Ebner, A.; Pastushenko, V. P.; Gruber, H. J.; Hinterdorfer, P., Nanomechanical recognition measurements of individual DNA molecules reveal epigenetic methylation patterns. *Nature Nanotechnology* **2010,** *5* (11), 788-791.

111. Pan, Y.; Wang, B.; Reese, R. A.; Xu, B., The molecular basis of interaction domains of full-length PrP with lipid membranes. *Nanoscale* **2019**.

APPENDIX A: AUTHOR'S BIBLIOGRAPHY

1. Reese, R.A.; Xu, B. Single-Molecule Detection of Proteins and Toxins in Food Using Atomic Force Microscopy. *Trends Food Sci. Technol.* **2019**, *83* (September 2017), 277–284.
2. Pan, Y.; Wang, B.; Reese, R. A.; Xu, B. The Molecular Basis of Interaction Domains of Full-Length PrP with Lipid Membranes. *Nanoscale* **2019**, DOI: 10.1039/c9nr02735a.
3. Song, B.; Kandapal, S.; Gu, J.; Zhang, K.; Reese, A.; Ying, Y.; Wang, L.; Wang, H.; Li, Y.; Wang, M.; et al. Self-Assembly of Polycyclic Supramolecules Using Linear Metal-Organic Ligands. *Nat. Commun.* **2018**, *9* (1), 4575.
4. Zhang, Z.; Wang, H.; Wang, X.; Li, Y.; Song, B.; Bolarinwa, O.; Reese, R. A.; Zhang, T.; Wang, X.; Cai, J.; et al. Supersnowflakes: Stepwise Self-Assembly and Dynamic Exchange of Rhombus Star-Shaped Supramolecules. **2017**, *30* (v).
5. Zhang, Y.; Zhang, M.; Reese, R.A.; Zhang, H.; Xu, B. Real-Time Single Molecular Study of a Pretreated Cellulose Hydrolysis Mode and Individual Enzyme Movement. *Biotechnol. Biofuels* **2016**, *9* (1), 85.
6. Brooks, K.; Yatvin, J.; McNitt, C. D **;** Reese, R. A.; Jung, C.; Popik, V. V.; Locklin, J. Multifunctional Surface Manipulation Using Orthogonal Click Chemistry. *Langmuir* **2016**, *32* (26), 6600–6605.